Constructing a Homodyne Detector for 399nm Laser light

Wayne Ströbel

Bachelorarbeit in Physik
angefertigt im Institut für Angewandte Physik

vorgelegt der
Mathematisch-Naturwissenschaftlichen Fakultät
der
Rheinischen Friedrich-Wilhelms-Universität
Bonn

November 2023

Ich versichere, dass ich diese Arbeit selbstständig verfasst und keine anderen als die angegebenen Quellen und Hilfsmittel benutzt sowie die Zitate kenntlich gemacht habe.

Bonn, 10.11.2023
Datum

Unterschrift

1. Gutachter: Prof. Dr. Sebastian Hofferberth
2. Gutachter: Dr. Frank Vewinger

Contents

CHAPTER 1

Introduction

With the development of increasingly large databases a need for better and more efficient ways of searching through these arises, as with modern computers finding a file inside a database of size N requires a computation time of order $O(N)$. It is possible to speed this process up to order $O(\sqrt{N})$ using quantum computers by running the Grover's algorithm [1]. Different to classical computers, which use transistors to run logical operations using bits, quantum computers require gate operations on qubits. In contrast to classical bits, these can not only be either 0 or 1, but rather can be a super position of both. One of the many challenges of running quantum computers are the limited coherence times of qubits [2], which makes communication between different systems separated over larger distances difficult. One way to tackle this challenge is by using photons. Photons inherently do not interact with other photons, though this can be achieved using methods of nonlinear quantum optics. [3]

At the Ytterbium Rydberg Nonlinear Quantum Optics experiment in Bonn the manipulation and interaction between single photons using Rydberg-Rydberg interactions between single atoms in an ultracold Ytterbium gas is investigated. With this the dynamics of a strongly interacting quantum system are mapped onto freely propagating photons, which can then be analyzed. In order to measure the single photons there are already two setups using heterodyne detection methods which measure conditional phase shifts introduced by the medium [4], [5], [6],[7]. The phase is measured as it contains information about how the photons have interacted with the given medium. We aim to now go one step further with homodyne detection. This gives the possibility to reconstruct the density matrix and wigner function of the created single photons[8]. To do this I follow the setup from Dr. Alexei Ourjoumtsev's laboratory in Collège de France in Paris for 795 nm laser light [9], but using 399 nm laser light, as we use a 2-photon transition of Ytterbium from the ground state to a Rydberg state with 399 nm and 395 nm.

In this thesis I characterize a specific balanced photo diode to figure out, if the homodyne setup is feasible to reconstruct for 399 nm laser light. For this I first give an insight in the theoretical background of homodyne detection and noise characterization in chapter 2. I then describe the full homodyne setup in the first part of chapter 3, followed by a simpler setup to compare the conversion gains given by the photo diode data sheet and measured values. In the next step I analyze the full setup with equal powers in probe and local oscillator beam to create a prediction model with which I

can align the setup when taking the probe beam to low beam powers. In the last step I check the phase stability of the setup to determine whether it suffices to passively scan the phase or if it is necessary to implement phase controls. In chapter 4 I discuss the results and give possible improvements and further perspectives.

CHAPTER 2

Theory

2.1 Interferometry

The following theoretical background is taken from "Quantum Optics: an Introduction" by Mark Fox [10].

2.1.1 Classical Interferometer

Interference can be seen when dividing light waves and recombining them with a phase difference. A well known experiment for this is the Mach-Zehnder-Interferometer, as seen in Figure 2.1. Assuming

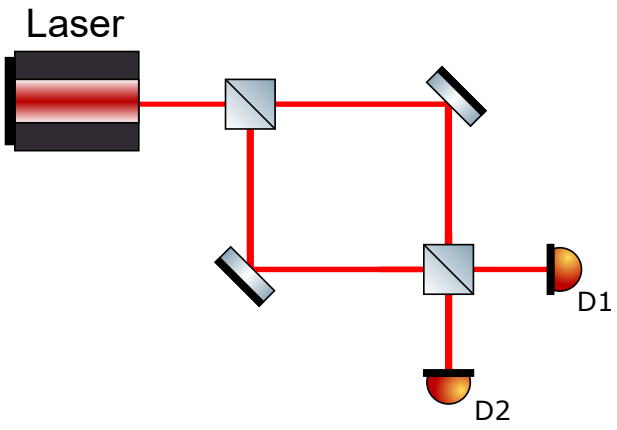

Figure 2.1: Mach Zehnder Interferometer with two beamsplitters, the top left being of variable splitting ratio and the bottom right being a 50:50 splitter.

equal path lengths, the electric fields ϵ_1 and ϵ_2 at the two detectors can be written as an overlap of

reflected and transmitted beams ϵ_r and ϵ_t of the first beamsplitter on the second 50:50 beamsplitter

$$\epsilon_1 = \frac{1}{\sqrt{2}}(\epsilon_t + \epsilon_r) \tag{2.1}$$

$$\epsilon_2 = \frac{1}{\sqrt{2}}(\epsilon_t - \epsilon_r). \tag{2.2}$$

Using the splitting ratio of the first beam splitter this can be rewritten using

$$\epsilon_t = t * \epsilon_0 \tag{2.3}$$

$$\epsilon_r = r * \epsilon_0 \tag{2.4}$$

$$\tag{2.5}$$

where r, t are the complex reflection and transmission coefficients which require $|r|^2 + |t|^2 = 1$, to

$$\epsilon_1 = \frac{1}{\sqrt{2}}(t\epsilon_0 + r\epsilon_0) \tag{2.6}$$

$$\epsilon_2 = \frac{1}{\sqrt{2}}(t\epsilon_0 - r\epsilon_0). \tag{2.7}$$

Introducing a phase shift on the transmitted beam allows us to control the interference at the detectors.

$$\epsilon_1 = \frac{\epsilon_0}{\sqrt{2}}(te^{i\Phi_t} + r) \tag{2.8}$$

$$\epsilon_2 = \frac{\epsilon_0}{\sqrt{2}}(te^{i\Phi_t} - r). \tag{2.9}$$

2.1.2 Stepping towards homodyning

Let us now identify the transmitted beam as the Local Oscillator and the reflected beam as the Probe beam. We can rewrite Equation 2.8 and 2.9 as

$$\epsilon_1 = \frac{1}{\sqrt{2}}(\epsilon_{LO}e^{i\Phi_{LO}} + \epsilon_s) \tag{2.10}$$

$$\epsilon_2 = \frac{1}{\sqrt{2}}(\epsilon_{LO}e^{i\Phi_{LO}} - \epsilon_s). \tag{2.11}$$

Additionally we can rewrite the probe beam as parts of it's quadratures using

$$\epsilon_s = \epsilon_s^{X_1} + i\epsilon_s^{X_2} \tag{2.12}$$

to give us

$$\epsilon_1 = \frac{1}{\sqrt{2}}((\epsilon_{LO}\cos\Phi_{LO} + \epsilon_s^{X_1}) + i(\epsilon_{LO}\sin\Phi_{LO} + \epsilon_s^{X_2})) \tag{2.13}$$

$$\epsilon_2 = \frac{1}{\sqrt{2}}((\epsilon_{LO}\cos\Phi_{LO} - \epsilon_s^{X_1}) + i(\epsilon_{LO}\sin\Phi_{LO} - \epsilon_s^{X_2})). \tag{2.14}$$

If we now subtract the two intensities at both detectors from each other we get a differential intensity of

$$i_{\text{diff}} \propto i_1 - i_2 \tag{2.15}$$
$$\propto \epsilon_1 \epsilon_1^* - \epsilon_2 \epsilon_2^* \tag{2.16}$$
$$\propto \sqrt{2}\epsilon_{\text{LO}}(\epsilon_{\text{s}}^{X_1} \cos\Phi_{\text{LO}} + \epsilon_{\text{s}}^{X_2} \sin\Phi_{\text{LO}}). \tag{2.17}$$

We can therefore scan the two quadratures of the probe beam simply by rotating the phase of the local oscillator.

2.1.3 Single photon Interferometry

Following Chapter 13 from "Getting Started in Quantum Optics" by Ray LaPierre [11] and replacing the classical fields with a wave function $\left|\Psi_{\text{in}}\right\rangle = \left|\Psi\right\rangle_1 \left|\alpha_{\text{LO}}\right\rangle$, using $\hat{a}$ and $\hat{a}^\dagger$ to describe the beam splitter and $< n_{1,2} >= \left\langle \Psi_{\text{out}} \right|_{1,2} \hat{a}^\dagger \hat{a} \left|\Psi_{\text{out}}\right\rangle_{1,2}$ as a photon count, we can derive the two outputs to be

$$\left\langle n_1 \right\rangle = \left\langle \Psi_{\text{in}} \right| \frac{1}{2} \left(\hat{a}_1^\dagger \hat{a}_1 - \hat{a}_1^\dagger \hat{a}_2 - \hat{a}_2^\dagger \hat{a}_1 + \hat{a}_2^\dagger \hat{a}_2 \right) \left|\Psi_{\text{in}}\right\rangle \tag{2.18}$$
$$\left\langle n_2 \right\rangle = \left\langle \Psi_{\text{in}} \right| \frac{1}{2} \left(\hat{a}_1^\dagger \hat{a}_1 - \hat{a}_1^\dagger \hat{a}_2 - \hat{a}_2^\dagger \hat{a}_1 + \hat{a}_2^\dagger \hat{a}_2 \right) \left|\Psi_{\text{in}}\right\rangle . \tag{2.19}$$

Therefore the homodyne signal becomes:

$$signal \propto \left\langle n_1 \right\rangle - \left\langle n_2 \right\rangle \tag{2.20}$$
$$\propto \left\langle \alpha_{\text{LO}} \right|_2 \left\langle \Psi \right|_1 \left(\hat{a}_1^\dagger \hat{a}_2 + \hat{a}_2^\dagger \hat{a}_1 \right) \left|\Psi\right\rangle_1 \left|\alpha_{\text{LO}}\right\rangle_2 \tag{2.21}$$
$$\propto \left\langle \Psi \right| \left(\alpha_{\text{LO}} \hat{a}_1^\dagger + \alpha'_{\text{LO}} \hat{a}_1^\dagger \right) \left|\Psi\right\rangle . \tag{2.22}$$

Using $\alpha_{\text{LO}} = |\alpha_{\text{LO}}| e^{i\Phi_{\text{LO}}}$, the Euler relation and the definition for the quadrature operators

$$\hat{Q} = \frac{1}{\sqrt{2}} \left(\hat{a} + \hat{a}^\dagger \right) \tag{2.23}$$
$$\hat{P} = \frac{-\mathrm{i}}{\sqrt{2}} \left(\hat{a} - \hat{a}^\dagger \right) \tag{2.24}$$

we get

$$\left\langle n_1 \right\rangle - \left\langle n_2 \right\rangle = \sqrt{2} |\alpha_{\text{LO}}| [\cos\Phi_{\text{LO}} \left\langle \Psi \right| \hat{Q} \left| \Psi \right\rangle + \sin\Phi_{\text{LO}} \left\langle \Psi \right| \hat{P} \left| \Psi \right\rangle]. \tag{2.25}$$

As seen before, the two quadratures can be measured by scanning the phase of the local oscillator. In the case of $|\Psi\rangle = |\alpha\rangle$ being a coherent state with eigenvalue $\alpha = |\alpha| e^{\mathrm{i}\Phi}$. The two quadratures Q and P correspond to the real and imaginary parts of α.

2.2 Homodyne vs Heterodyne Detection

One of the key differences between homodyne and heterodyne detection is that with heterodyning, the local oscillator and probe beam are detuned in order to see a beat note signal, which can then be compared to a reference signal. This allows a conditional phase to be measured. In homodyning

the local oscillator and probe beam are mode matched. Taking short measurements over 100 µs while the phase of the local oscillator is scanned, gives information on the quadratures, with which either a density matrix or a Wigner function can be recreated using a maximum likelihood estimation algorithm.

2.3 Noise Characterization

For light systems there are different types of noise. There is white noise, which corresponds to a constant shift in noise, shot noise, which stems from the poissonian nature of photons, and technical noise, which behaves as $\sigma^2_{\text{technical}} \propto P^2$. Shot noise is defined as

$$\sigma^2_{\text{shot}} = 2eI\Delta\nu \tag{2.26}$$

with e being the electron charge, I the current signal and $\Delta\nu$ the limiting bandwidth. For our purposes, we need to rewrite the current I to the incoming laser power P. For this we consider the amount of electrons being created for a specific laser power P. This can be written as

$$I = \frac{Pe}{\hbar\omega} \tag{2.27}$$

where ω is the frequency of the used laser light. As the detector itself has a limited efficiency, we need to additionally include a quantum efficiency term η_0. With this, the shot noise can be written as

$$\sigma^2_{\text{shot}} = \eta_0 \frac{Pe^2}{\hbar\omega} 2\Delta\nu. \tag{2.28}$$

As we wish to have the shot noise given in terms of voltage, we use the trans-impedance gain G_0 of the used detector in order to convert from current to voltage, giving us

$$\sigma^2_{\text{shot,V}} = \eta_0 \frac{Pe^2}{\hbar\omega} 2G_0^2\Delta\nu. \tag{2.29}$$

Finally, as the photo current hitting the detector will be dominated by the local oscillator beam, we can neglect the probe beam $P = P_{\text{LO}}$, finally giving us

$$\sigma^2_{\text{shot}} = \frac{\eta_0 P_{\text{LO}} e^2}{\hbar\omega} 2G_0^2\Delta\nu. \tag{2.30}$$

CHAPTER 3

Experiment

In this Chapter I first discuss the full experimental setup I recreate. I then start by characterizing the used Balanced Photo Detector (BPD) using the given data sheet, followed by the aligning procedure of the Interferometer for the Homodyne Detector and ending with the noise characterization of the Interferometer.

3.1 Overview of the experimental setup

The homodyne detector setup as presented in Figure 3.1 is based on the setup from Alexei Ourjoumtsev's laboratory in Collège de France in Paris [8], which can be seen in Figure 3.2. Starting at the fibre, we couple p-polarized light at 399 nm (see chapter 1) taken from the laser table of the YQO experimental setup and send it onto a polarized beam splitter (PBS) in order to clean the polarization. After this the light is sent onto a beam splitter (BS) which divides the beam into two arms: the local oscillator (LO, dark blue beam), as a classical beam, and the Probe beam (light blue beam), which lies in the few photon regime. Next, following the path of the beam, the AOMs are used to control the frequency and intensity of the light. The faraday isolator in the probe beam ensure that there is no back-scattered light that gets coupled back into the fibre, as it could interfere with the YQO experimental setup. By aligning the Probe and LO beam on the two inputs of the beam splitter, an interference signal is generated at the outputs of the BS. As seen in chapter 2, it is important for the detector to receive two balanced inputs. To focus the beams onto the photo diodes, we use concave mirrors, as using lenses would introduce further losses in laser power. The photo diodes are additionally hit at an angle. This allows us to power balance the detector firstly by angle tuning the inputs, and secondly using a $\lambda/2$-plate plate to introduce controlled reflections. This works as the laser hits the diodes close to the Brewster angle, where p-polarized light is transmitted, whilst s-polarized light is reflected. Afterwards, we can measure short signals on the BPD on the scale of 100 µs for multiple different phases, either by passively scanning if the phase drift of the interferometer allows it, or by using the AOMs to shift the phase for each measurement. These measurements give us information on the quadratures depending on the phase, as seen in Equation 2.25. After taking enough measurements these can be fed into a maximum-likelihood algorithm to reconstruct the density matrices and wigner functions of the probe beam [9]. The short measurements that are used for the quantum state reconstruction go past the scope of this thesis.

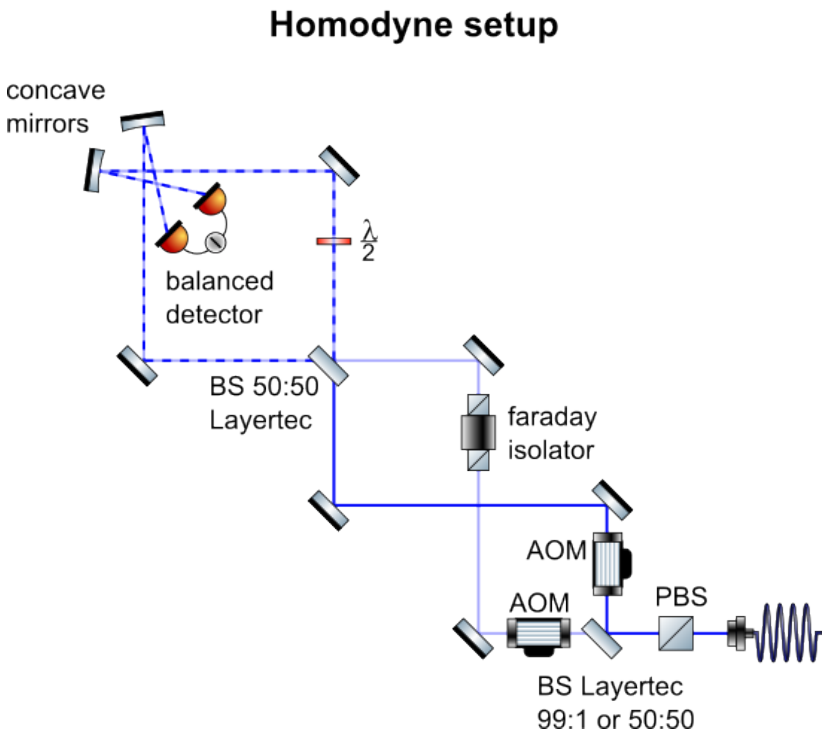

Figure 3.1: Homodyne setup using a single input, split into a local oscillator beam (dark blue) and a probe beam (light blue) with AOMs used to control intensity and frequency of the beams, aligned on an interferometer, focused onto the BPD

3.2 Characterization of Balanced PDs

Before starting work on creating the proper homodyne setup, the Balanced Detector needs to be characterized. For this I use the setup as seen in Figure 3.3. The incoming laser beam is first sent onto a $\lambda/2$-plate , followed by a PBS in order to prepare a clean p-polarized beam. As in this setup the photo diodes are hit straight on, I use an angled glass plate to mimic the angled diodes. This way I can once again fine tune the balancing using a $\lambda/2$-plate . The lenses are placed in a way such that the entire beam hits the most amount of area of the photo diode. The Detector itself has three different outputs, two outputs to monitor the individual photo diodes called Monitor+ and Monitor-, and an RF output which is an amplified signal resulting from the subtraction of both photo diodes.

Alignment and balancing Let's start with the alignment of the beam onto the detector. I aligned the beam by first using an iris mounted to the detector, such that the beam is orthogonal to the detector plane. I then fix the lenses with a focal point $f = 75\,\text{mm}$ at a distance close to the focal point. When looking at the monitor output signal using an oscilloscope, scanning the x and y axes using the previous mirror we can see a plateau with a rising and a falling edge. We fix the distance of the lens in such a way, that the area of the edges and the plateau all roughly take up a third of the entire signal area. This is done for both lenses. This results in having most of the photo diode covered by the beam, without cutting off a large portion of the beam. In order to properly center both beams on the detector, I look

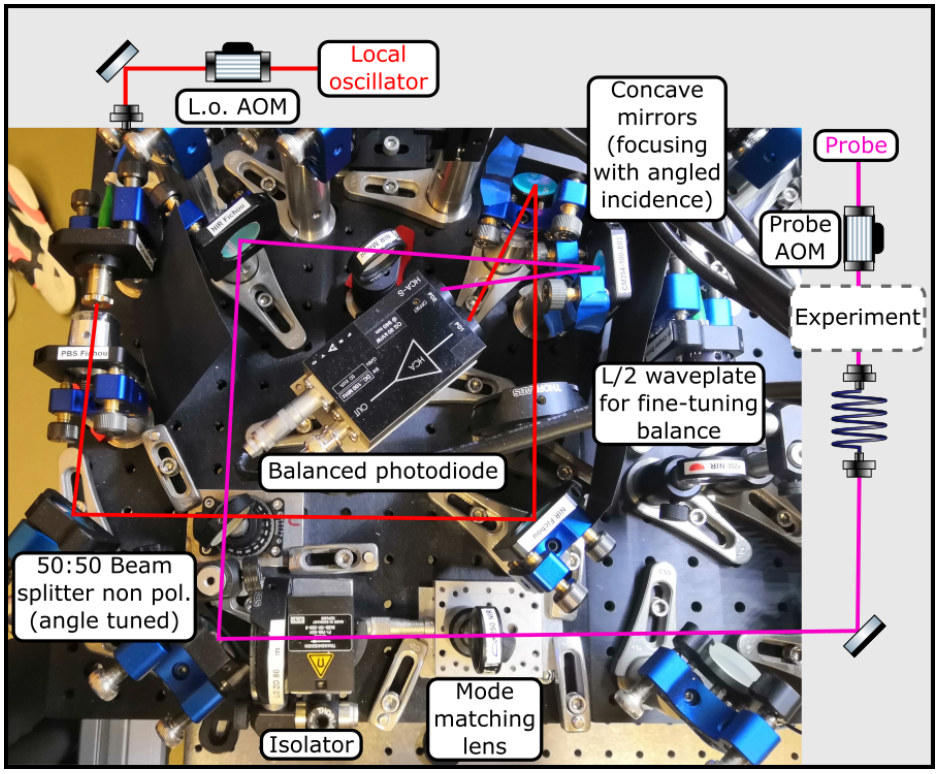

Figure 3.2: Homodyne detector setup of Alexei Ourjoumtsev's laboratory in Collège de France in Paris for 795 nm laser light, which we base our setup in Figure 3.1 off of, with an additional mode matching lens, and a Probe beam coming from an atom cloud, opposed to dividing a single laser.

at the RF output using the oscilloscope and find, that when scanning the area of the plateau, I get a maximum (or minimum, depending on which photo diode is being used) at a point that corresponds to the beam being centered on the diode. With a now properly aligned detector, I start balancing it. First I check the offset of the detector when no light hits the photo diodes. This is called the dark noise signal of the detector. The detector is properly balanced, when the offset of the RF signal, with laser light, equals the offset of the dark noise RF signal. Using the optimally aligned setup, I characterize the BPD.

Calculating characteristic values of the detector As this type of detector has yet to be used in the research group, we wish to know the characteristics of the detector, and how these deviate from the specifications given by the manufacturer. Additionally this allows us to make predictions on how the detector behaves for a given input, which will be used at a later stage for further alignment processes. I begin by checking a few specifications given on the data sheet of the detector[1] , mainly the RF and monitor output conversion gain and the responsivity. From these values I can calculate the expected

[1] Detector/Model: Thorlabs Free-Space Balanced Amplified Photo detector / PDB230A

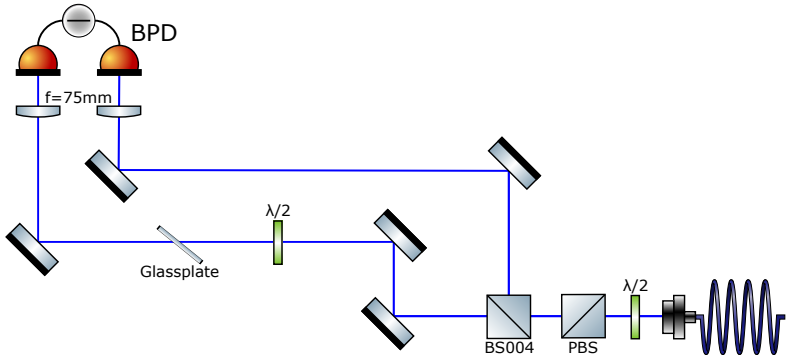

Figure 3.3: Setup without the interferometer and using only the local oscillator to characterize characteristic detector values and noise, as described in section 3.2

Table 3.1: BPD specific characterising values taken from the thorlabs datasheet [1]

RF Output Conversion Gain	$G_{\text{conv}}^{\text{RF}}$	26.5×10^3 V/W @ 820 nm
Monitor Output Conversion Gain	$G_{\text{conv}}^{\text{Mon}}$	10 V/mW @ 820 nm
Max Responsivity	$R(\lambda)$	0.53 A/W @ 820 nm
		0.15 A/W @ 399 nm

trans impedance gain using the formula given in the data sheet:

$$G_{\text{TI}}^{\text{Mon}} = \frac{G_{\text{conv}}^{\text{Mon}}}{R(820\,\text{nm})} = 18\,868\,\text{V/A} \tag{3.1}$$

$$G_{\text{TI}}^{\text{RF}} = \frac{G_{\text{conv}}^{\text{RF}}}{R(820\,\text{nm})} = 50\,000\,\text{V/A}. \tag{3.2}$$

As this value is wavelength independent I use it to calculate the expected conversion gains for 399 nm:

$$G_{\text{conv}}^{Mon}(399\,\text{nm}) = R(399\,\text{nm}) \cdot G_{\text{TI}} = 2.83\,\text{V/mW} \tag{3.3}$$

$$G_{\text{conv}}^{RF}(399\,\text{nm}) = R(399\,\text{nm}) \cdot G_{\text{TI}} = 7.5\,\text{V/mW}. \tag{3.4}$$

Additionally I calculate the expected quantum efficiency of the detector at 399 nm by dividing the Responsivity R at 399 nm by the Responsivity $\mathcal{R}$ for the case of one photon creating one electron. Let us first calculate the Responsivity $\mathcal{R}$ for 399 nm in the case of 100 % quantum efficiency:

$$\mathcal{R}(399\,\text{nm}) = \frac{e^-}{\gamma_{399\,\text{nm}}} = \frac{1.602 \times 10^{-19}\,\text{C}}{4.98 \times 10^{-19}\,\text{J}} = 0.322\,\text{A/W}.\mathcal{R}(820\,\text{nm}) = 0.661\,\text{A/W} \tag{3.5}$$

Using this I get:

$$QE = \frac{R(399\,\text{nm})}{\mathcal{R}} = 46.6\,\%. \tag{3.6}$$

Comparing this to the quantum efficiency given for 820 nm ,with a responsivity $R(820\,\text{nm}) = 0.53\,\text{A/W}$, of $QE = 80.2\,\%$, we see that the efficiency for the blue is much lower than for infrared. This loss can be seen in form of reflections on the surface of the detector. This also means that we can "increase" the efficiency by reflecting and refocusing the reflected light back onto the detector.

Measuring characteristic values of the detector Using these expected values I now measure them with the setup seen in Figure 3.3 to see if the detector full fills the expectations. To measure the Conversion Gains of the Monitors, I use

$$G_{\text{conv}} = \frac{I_{\text{in}}}{U_{\text{osci}}} \tag{3.7}$$

where I_{in} is the laser power measured infront of the PDs and U_{osci} is the voltage measured on the oscilloscope. The RF Conversion Gain is measured by blocking one of the PDs, making sure not to saturate the amplified RF Output. The results are found in Table 3.2. Whilst the monitor conversion

Table 3.2: Comparison between data sheet values at 820 nm and the measured values at 399 nm

	820 nm	399 nm expected	399 nm measured
$G_{\text{conv}}^{\text{RF}}$	26.5 V/mW	7.5 V/mW	(6.56 ± 0.37) V/mW
$G_{\text{conv}}^{\text{Mon}}$	10 V/mW	2.83 V/mW	(2.75 ± 0.10) V/mW
$\frac{G_{\text{conv}}^{\text{RF}}}{G_{\text{conv}}^{\text{Mon}}}$	2.65	—	(2.39 ± 0.12)

gain G_{conv}^{Mon} is inside a one sigma uncertainty, the RF conversion gain G_{conv}^{RF} is off by roughly 3 sigma.This is a significant deviation from the specified value, which could stem from slightly deviating amplifier values, caused by voltage deviations or production impurities. It doesn't pose any further issues, as this deviation is now known and can be taken into account for at later stages.

3.2.1 Detector noise characterization

Next we would like to know how the detector noise behaves for different laser powers, if the detector full fills it's specified bandwidth of 100 MHz and if we are in the shot noise regime for the laser powers we are using. For this I will look at the noise spectrum of the detector for different laser powers and frequency ranges. I do this by measuring the RF output using a spectrum analyzer. We chose the frequency ranges to be 0...150 MHz and 0...10 MHz . These ranges are chosen specifically for one to look at the full bandwidth of the detector and the other to look at the frequency range that would be used for the state reconstruction. The used spectrum analyzer and it's settings are described in Appendix A.

Measured spectrum with power-balanced beams Let's start with the 0...150 MHz Range. We expect to see a flat spectrum, which falls off about −3 dB at 100 MHz due to the bandwidth. For increasing laser powers we expect the spectrum to be shifted upwards, as the intensity noise scales proportionally to the intensity. The data can be found in Figure 3.4. Here we can see a couple of things: starting with the far left, we can see the expected $1/f$-noise. After this we can see the increased amplitude of the signals for rising laser power, in addition to a spectrum of the spectral analyzer

instrument noise. Additionally there is a bump at around 100 MHz, which stems from the detector, as it can't be seen in the instrument noise spectrum. I subtract the measured dark noise, as can be seen in Figure 3.5, to get a nice plateau up to around 70 MHz, with the signals dropping about 3 dBm until 100 MHz, which corresponds to the expected bandwidth of 100 MHz of the BPD. We can also see some sharp peaks in the spectrum, which will be discussed later. The 1.05 mW laser power spectrum fluctuations can be attributed to a problem with saving the data on the spectrum analyzer. The data is left in for completeness. Moving on to the 0...10 MHz Range, which can be found in Figure 3.6.

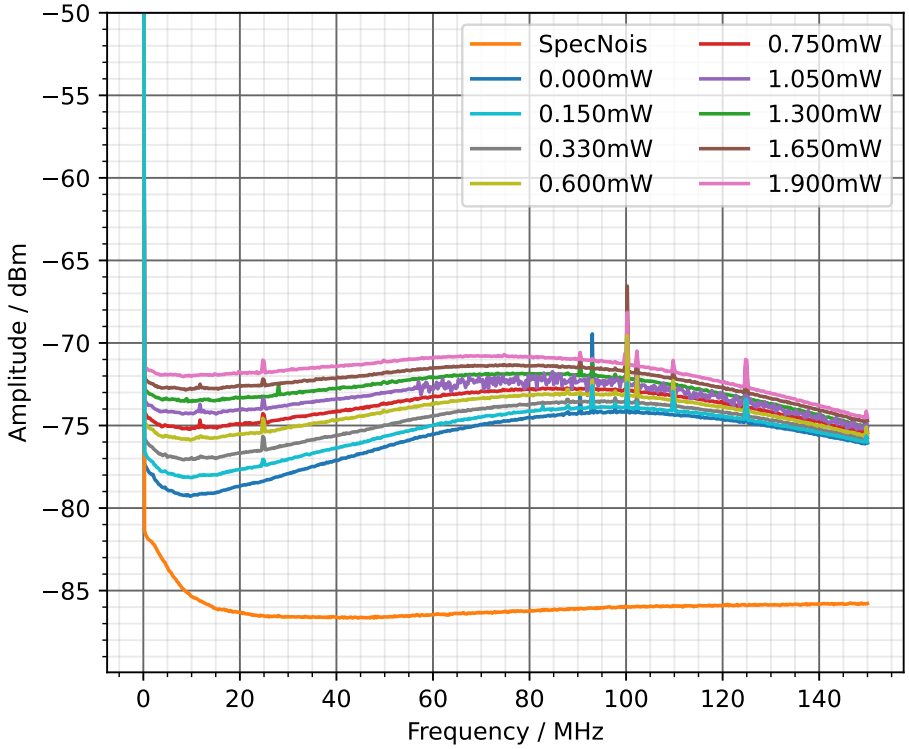

Figure 3.4: Visualized raw data from the balanced Detector Setup with a range of 0...150 MHz for the spectrum analyzer instrument noise and different laser powers. The y-axis corresponds to the noise amplitude given in dBm and the x-axis to the frequency given in MHz

As can be seen already in the 0...150 MHz spectrums, this part of the spectrum is flat, with only the $1/f$-noise which can be seen on the left hand side. Removing the dark noise again (see Figure 3.7) leads to a plateau of varying height based on the laser power. As the range is small, we don't notice any drop in signal towards higher frequencies. In this spectrum we don't see any of the sharp peaks, apart from the highest laser power.

Some interesting aspects in both Figure 3.4 and 3.6 are the peaks at specific frequencies. We differentiate between peaks in the dark spectrum (0 mW) and in the other spectra. The peaks in the dark spectrum are caused by radio stations which are picked up and amplified by the detector itself. These peaks can also be seen in the other spectra. The peaks that are left in the spectra with incoming laser power stem from laser noise, which isn't completely suppressed in the detector. One example is

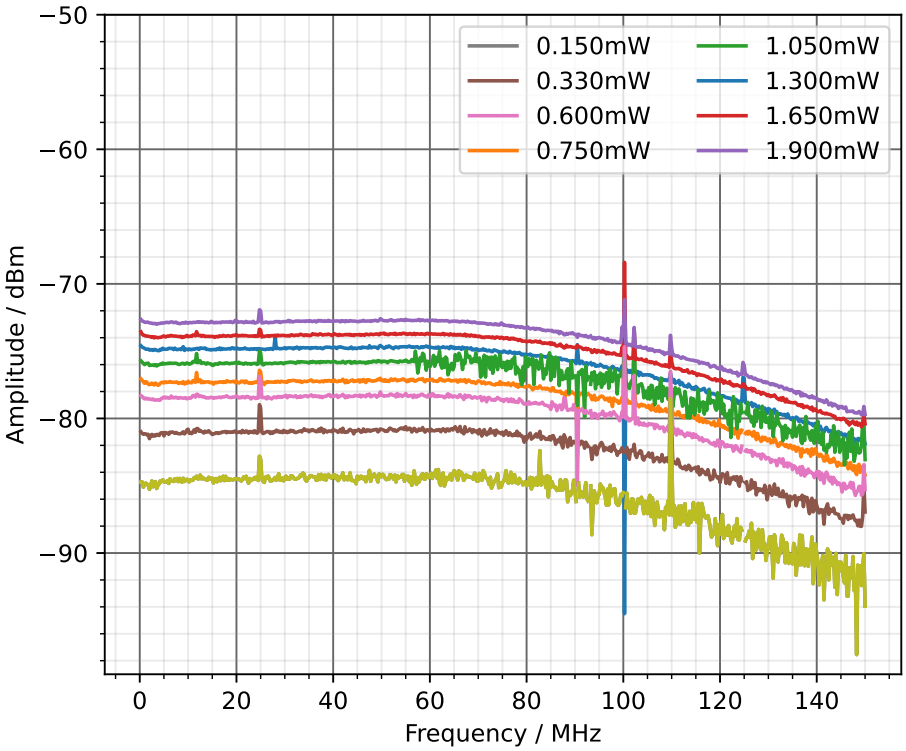

Figure 3.5: Visualized data with removed dark noise from the balanced Detector Setup with a range of 0...150 MHz for different laser powers. The y-axis corresponds to the noise amplitude given in dBm and the x-axis to the frequency given in MHz

at 25 MHz. These peaks can be more clearly seen in the fully unbalanced setup, i.e. by blocking one input.

Measured unbalanced spectrum with one beam blocked We want to look at the unbalanced spectra to more specifically see where the peaks in the balanced spectra come from. First looking at the 0...150 MHz range as seen in Figure 3.8, we see a very noisy spectrum, which is to be expected as none of the intensity noise is cancled out. Also we can see that the 1.3 mW laser power spectrum is almost equal to the Spectrum Analyzer noise. This is due to the detector being saturated. More importantly we can see a lot of sharp peaks at different frequencies, which are again not visible in the dark spectrum. Looking at 25 MHz we can see large peaks. From this I conclude, that the peaks stem from technical noise of the laser. When subtracting the dark noise we can also see a very strong $1/f$-noise contribution, which leads up to roughly 50 MHz. Let's take a closer look at the range in Figure 3.10. We can see two types of spectra, one for the powers from 0.07 mW to 0.6 mW, excluding 0.45 mW with sharp peaks and two (0.45 mW 1.3 mW with broad peaks. The spectra with broad peaks are caused by the laser going into multi mode, whilst the sharp peaks are in single mode. As we require the laser to be in single mode, the multi mode spectra don't give us any relevant information.

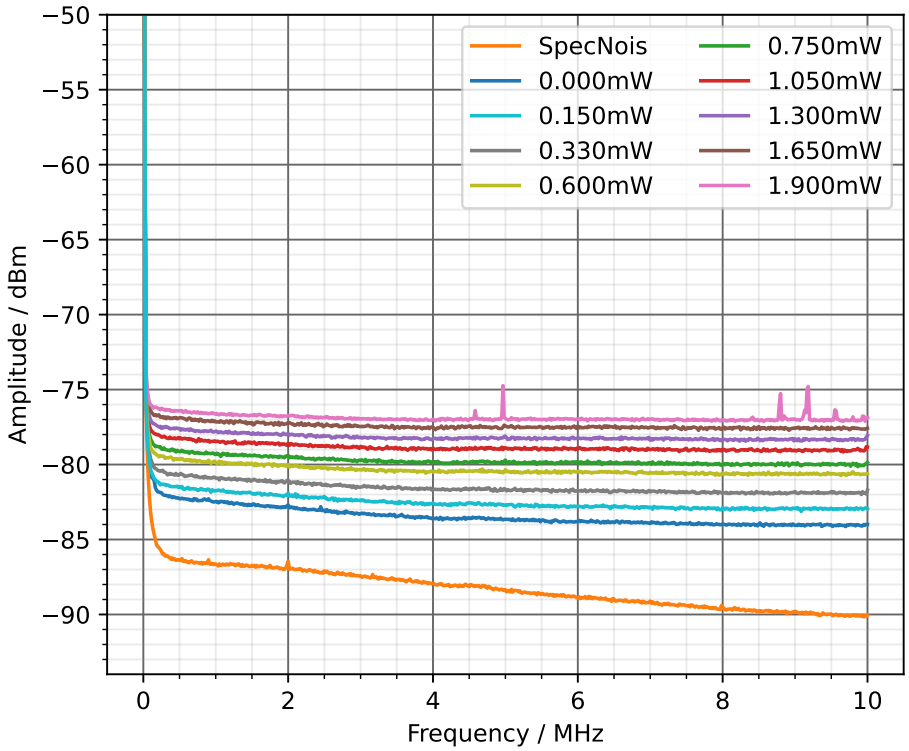

Figure 3.6: Visualized raw data from the balanced Detector Setup with a range of 0...10 MHz for the spectrum analyzer instrument noise and different laser powers. The y-axis corresponds to the noise amplitude given in dBm and the x-axis to the frequency given in MHz

Characterizing the detector shot noise Using Equation 2.30 and the values from section 3.2 I calculate the theoretical shot noise to be

$$(\sigma^2_{\text{shot}})_{0\ldots150\,\text{MHz}} = (18.4 \pm 0.2) \times 10^{-3}\,\mu\text{W/mW} \cdot P_{\text{LO}} \tag{3.8}$$

$$(\sigma^2_{\text{shot}})_{0\ldots10\,\text{MHz}} = (9 \pm 1) \times 10^{-3}\,\mu\text{W/mW} \cdot P_{\text{LO}} \tag{3.9}$$

with $\Delta\nu = 20\,\text{MHz}$ for the 0...150 MHz range and 10 MHz for the short range. Going back to the balanced spectra, I calculate the shot noise of the removed dark noise spectra of Figure 3.5 and 3.7. To do this I first need to convert dBm to W/Hz so I can integrate over the above mentioned ranges. This is explained in subsection A.1.1. The resulting noise powers are plotted against the used laser powers in order to see the shot noise of our setup (see Figure 3.12 and 3.13). As one can see, there is a linear relation between laser power and noise power, with a slope of $(8.31 \pm 0.05) \times 10^{-3}\,\mu\text{W/mW}$ for 0...10 MHz and $(16.6 \pm 0.2) \times 10^{-3}\,\mu\text{W/mW}$ for 0...150 MHz . The measured shotnoise coincides with the theoretical predictions, we are therefore in the shot noise limited regime. We can also see an increase in the noise power for the 1.9 mW laser power mesaurement, which could indicate the start of the technical noise regime.

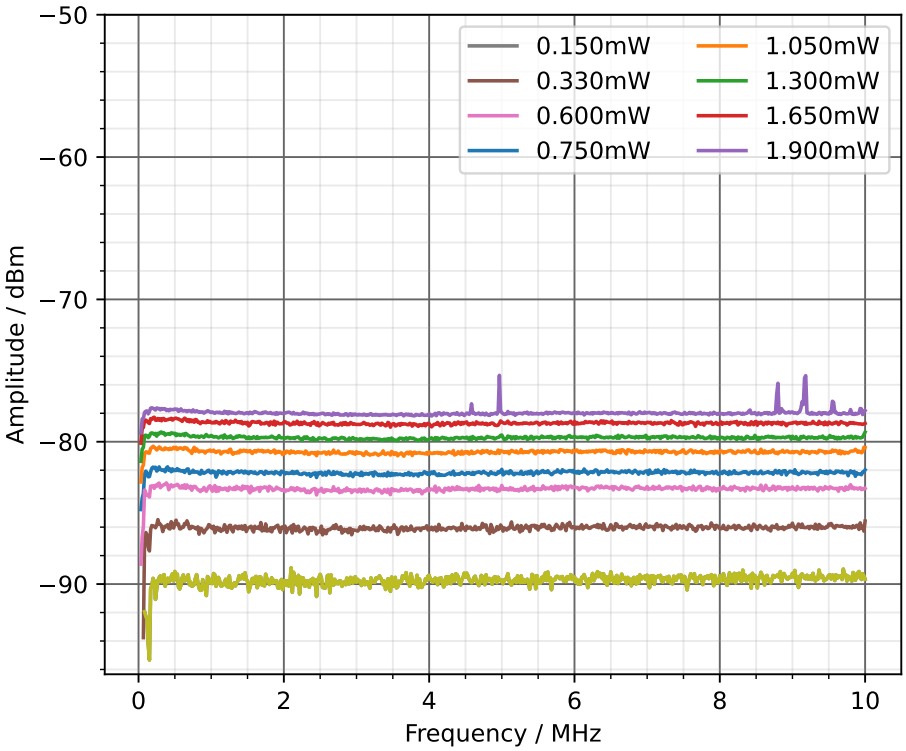

Figure 3.7: Visualized data with removed dark noise from the balanced Detector Setup with a range of 0...10 MHz for different laser powers. The y-axis corresponds to the noise amplitude given in dBm and the x-axis to the frequency given in MHz

3.3 Aligning Interferometer

Let us now head towards the proper homodyne setup.I do this in two steps, first I use the setup given in Figure 3.1 with the 50:50 beam splitter, as this allows me to characterize and optimize the alignment of both beams on the interferometer. The AOMs are used to introduce a detuning of 100 Hz such that we see a beat frequency. For two balanced inputs on the interferometer we theoretically expect a visibility of 100 %. I can therefore use this fact to mode match both beams on the interferometer. The used AOMs require a beam width of less than 0.45 mm. This results in a short Rayleigh length of about 0.5 m, which causes the beam to diverge quickly, as can be seen in Figure 3.14. The setup itself is only about 0.95 m long, which in turn means that the beam width at the end of the setup is roughly 4 times the size, which is still small enough for us to focus it onto the detector using concave mirrors.

3.3.1 Alignment using a 50:50 beam splitter

In order to see interference I need to properly mode match the two beams coming from the first 50:50 BS on the second beam splitter. I do this by first blocking one beam and aligning the probe beam such that the detector is balanced (see section 3.2). After this I unblock the beam and use the two mirrors in front of the second beam splitter to match the modes of both beams. Once the beam is roughly aligned I start seeing the interference on the oscilloscope. To precisely mode match I can now use

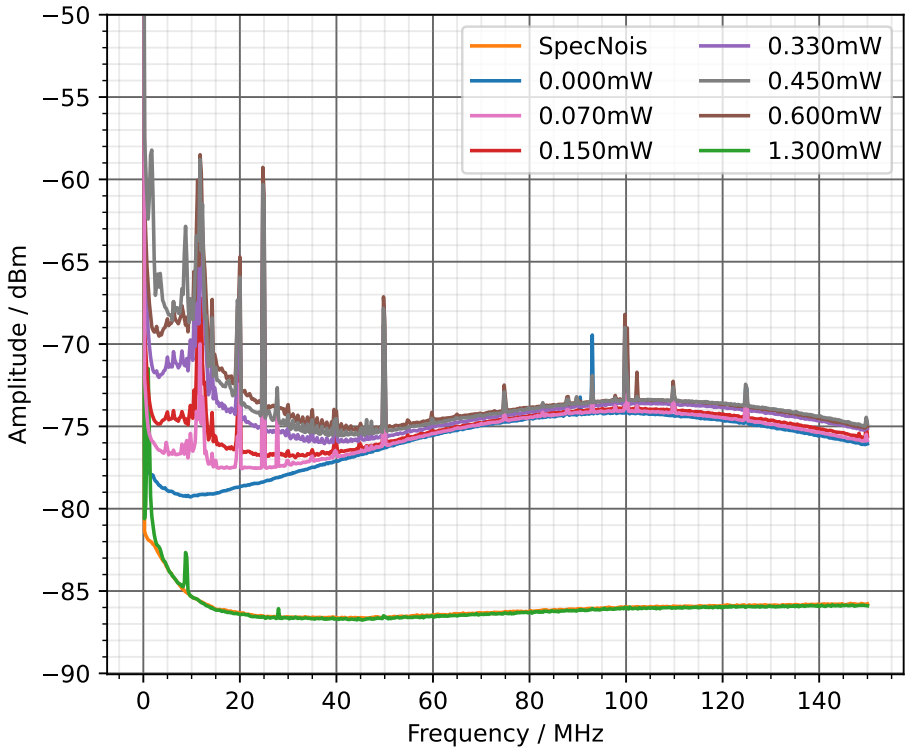

Figure 3.8: Visualized raw data from the fully balanced Detector Setup with a range of 0...150 MHz for the spectrum analyzer instrument noise and different laser powers. The y-axis corresponds to the noise amplitude given in dBm and the x-axis to the frequency given in MHz

the interference fringes as a measure of the quality of the matching. Optimally I would like a 100 % contrast in our interference. By optimizing the beam alignment I attempt to get as close as possible to the desired contrast.

Visibility After the alignment is as good as possible, I use the visibility to check the quality of the mode matching. The interference fringes for the aligned setup can be seen in Figure 3.15. Fitting some sinus functions with a constant shift to the data I calculate the visibility using

$$v = \frac{I_{\max} - I_{\min}}{I_{\max} + I_{\min}} \tag{3.10}$$

where $I_{\max}$ and $I_{\min}$ are given by

$$I_{\max} = c + A \tag{3.11}$$

$$I_{\min} = c - A \tag{3.12}$$

with the values from the fit, which are given in Table 3.3. Using these I calculate the visibility to be $v^{\text{Mon+}} = (99.7 \pm 0.1)$ % and $v^{\text{Mon−}} = (99.77 \pm 0.11)$ %, which correspond to almost the highest possible quality of mode matching. These values could be further improved by using precision tools,

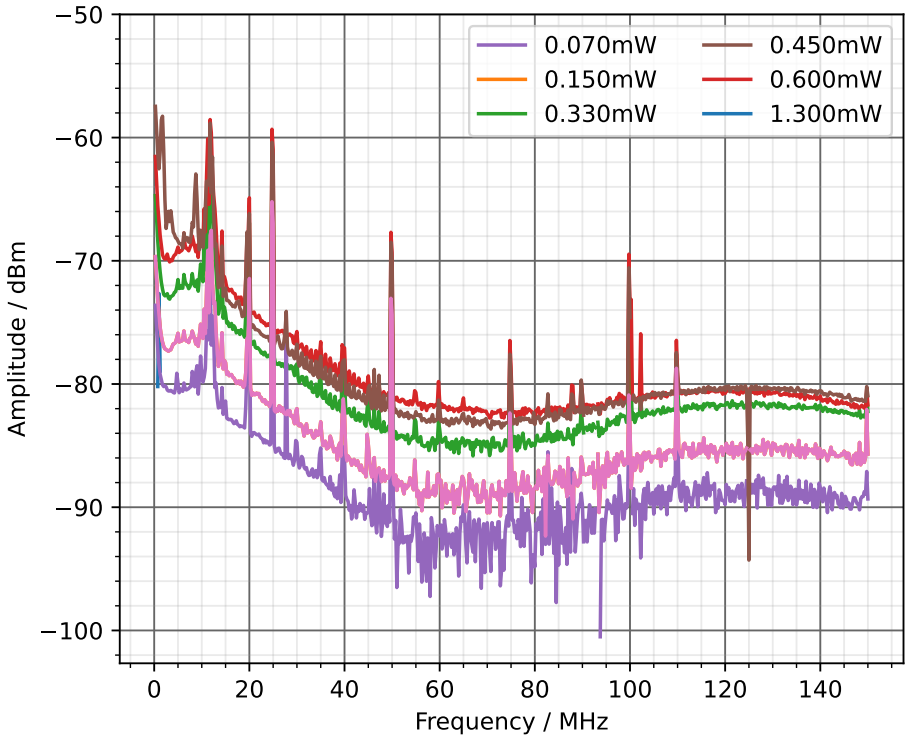

Figure 3.9: Visualized data with removed dark noise from the fully unbalanced Detector Setup with a range of 0...150 MHz for different laser powers. The y-axis corresponds to the noise amplitude given in dBm and the x-axis to the frequency given in MHz

Table 3.3: Sinus fit data for the calculation of the visibility from Figure 3.15 with fits of the form $y = A \sin(fx + \phi) + c$

Monitor-	
Amplitude A	(0.7748 ± 0.0006) V
Frequency f	(101.40 ± 0.02) MHz
shift ϕ	$(-1.0227 \pm 0.0005)\,\pi$
constant c	(0.7771 ± 0.0005) V
Monitor+	
Amplitude A	(0.7690 ± 0.0007) V
Frequency f	(101.40 ± 0.02) MHz
shift ϕ	$(-0.0210 \pm 0.0009)\,\pi$
constant c	(0.7708 ± 0.0005) V

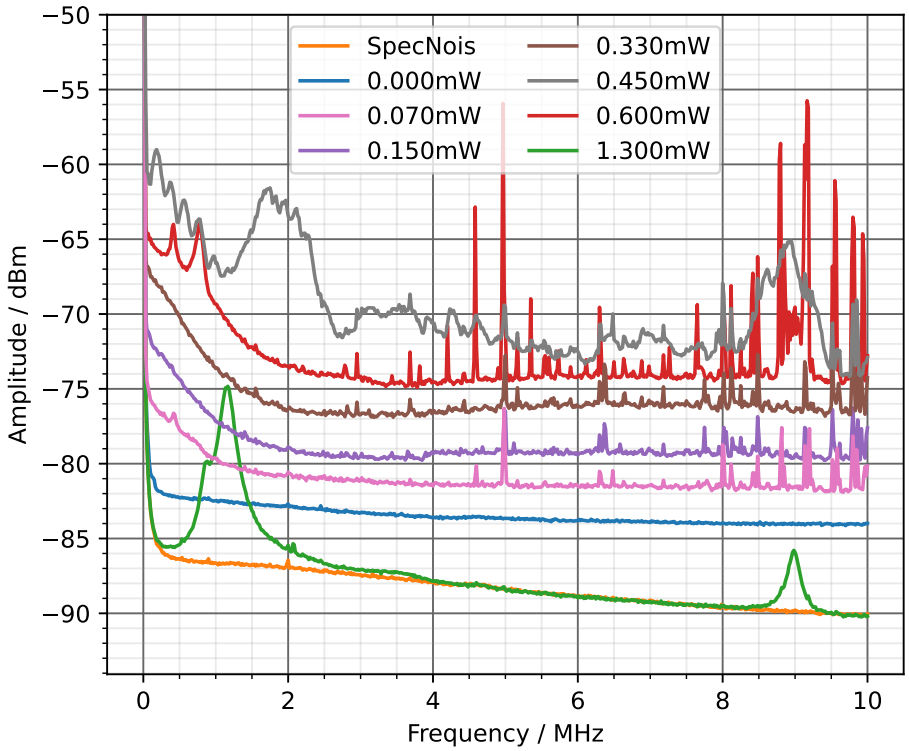

Figure 3.10: Visualized raw data from the fully balanced Detector Setup with a range of 0...10 MHz for the spectrum analyzer instrument noise and different laser powers. The y-axis corresponds to the noise amplitude given in dBm and the x-axis to the frequency given in MHz

but for hand adjusted mirrors they are sufficient enough to approximate the visibility as 1 in the later calibration calculations.

3.3.2 Calibration of interference signals

As a next step we would like to identify one beam as the Probe beam and reduce its intensity to low powers, so we will be using a 99:1 beam splitter instead of the 50:50 beam splitter. This is done to keep as much laser power in the LO beam as possible. As the expected visibility and thus the RF signal amplitude aren't easy to estimate without prior calibration, I made a prediction model that uses the input beam powers and the measured conversion of section 3.2 to calculate the maximum possible visibility based on the measurements presented in section 3.3. Using the conversion factors to convert incoming beam powers to measured voltages on the oscilloscope and formulas coming from the visibility of a interferometer we can derive the amplitude and frequency of the expected visibility,

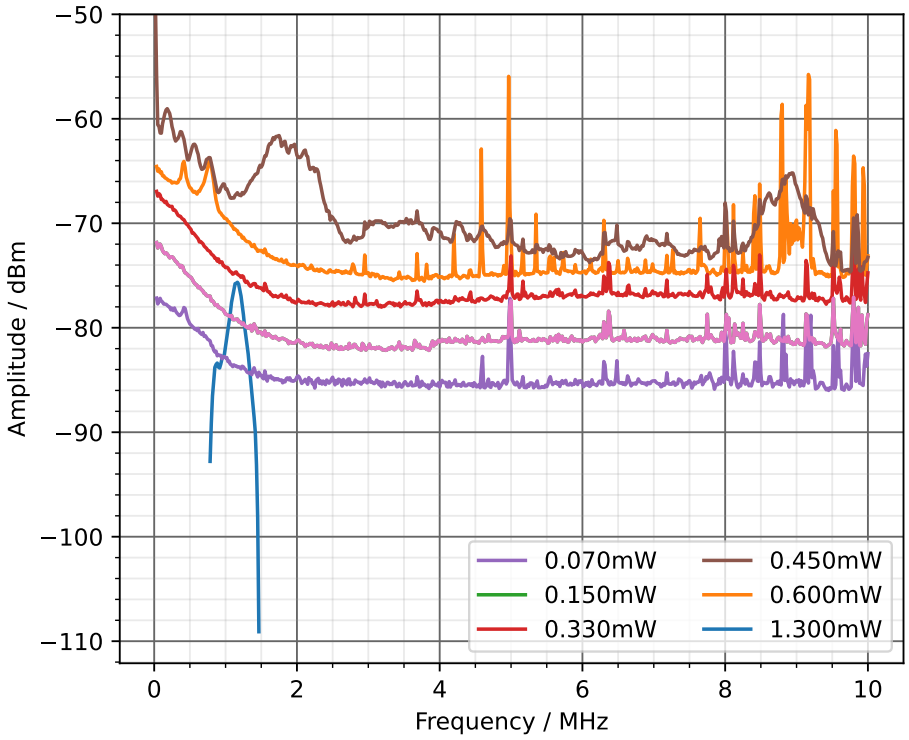

Figure 3.11: Visualized data with removed dark noise from the fully unbalanced Detector Setup with a range of 0...10 MHz for different laser powers. The y-axis corresponds to the noise amplitude given in dBm and the x-axis to the frequency given in MHz

starting from the incoming beam intensities I_1 and I_2 with respective frequencies f_1 and f_2:

$$I_{\max} = \frac{I_1 + I_2}{2}(1 + 2 \cdot \sqrt{\alpha(1-\alpha)}) \tag{3.13}$$

$$I_{\min} = \frac{I_1 + I_2}{2}(1 - 2 \cdot \sqrt{\alpha(1-\alpha)}) \tag{3.14}$$

$$\alpha = \frac{I_1}{I_1 + I_2}. \tag{3.15}$$

From this the amplitude of the Monitor outputs can be calculated using

$$A_{\text{Mon}} = G_{\text{conv}} Mon \left(I_{\max} - I_{\min}\right) \tag{3.16}$$

and of the RF output as

$$A_{\text{RF}} = G_{\text{conv}} RF \left(I_{\max} - I_{\min}\right). \tag{3.17}$$

with the frequency

$$f = |f_1 - f_2| \tag{3.18}$$

With this I can fit a sinus of the form $y = A \sin(\frac{2\pi x}{f})$, which corresponds to the maximum possible visibility for any two given beam powers, see Figure 3.16.

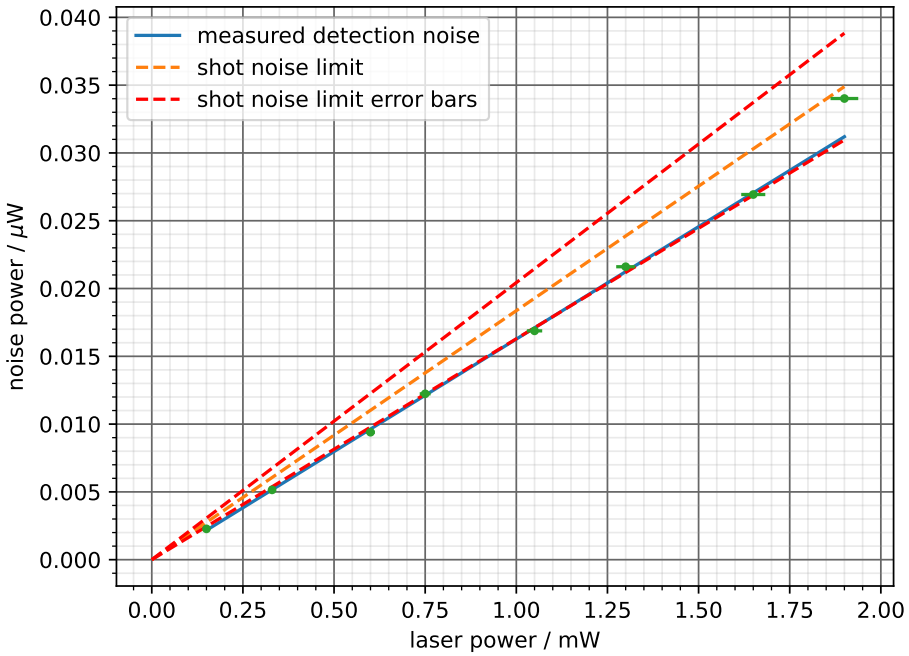

Figure 3.12: Shot noise in µW as calculated in section 3.2.1 plotted against laser power in mW for 0...150 MHz range with included theoretical lower shot noise limit.

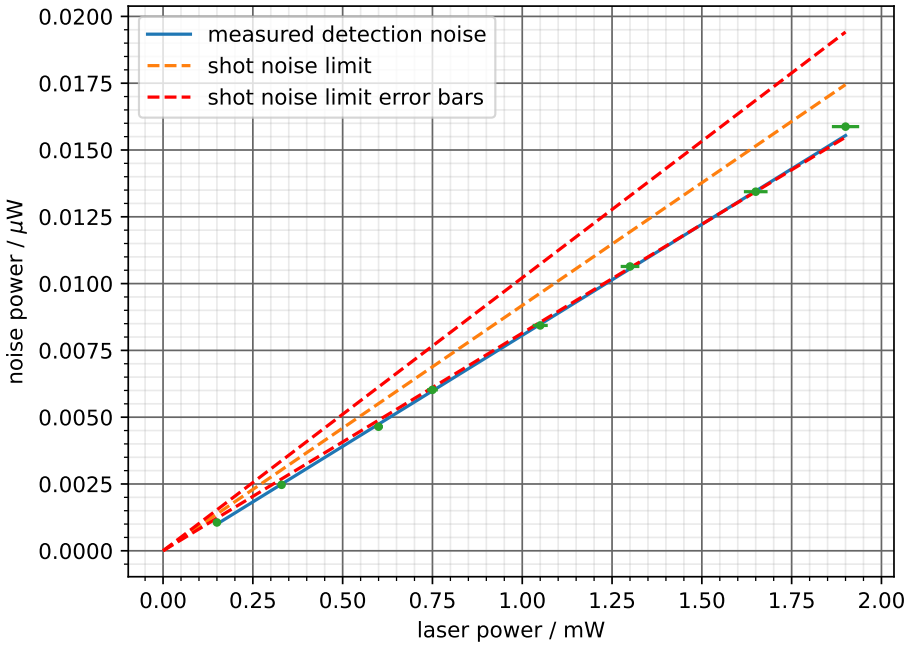

Figure 3.13: Shot noise in µW as calculated in section 3.2.1 plotted against laser power in mW for 0...10 MHz range with included theoretical lower shot noise limit.

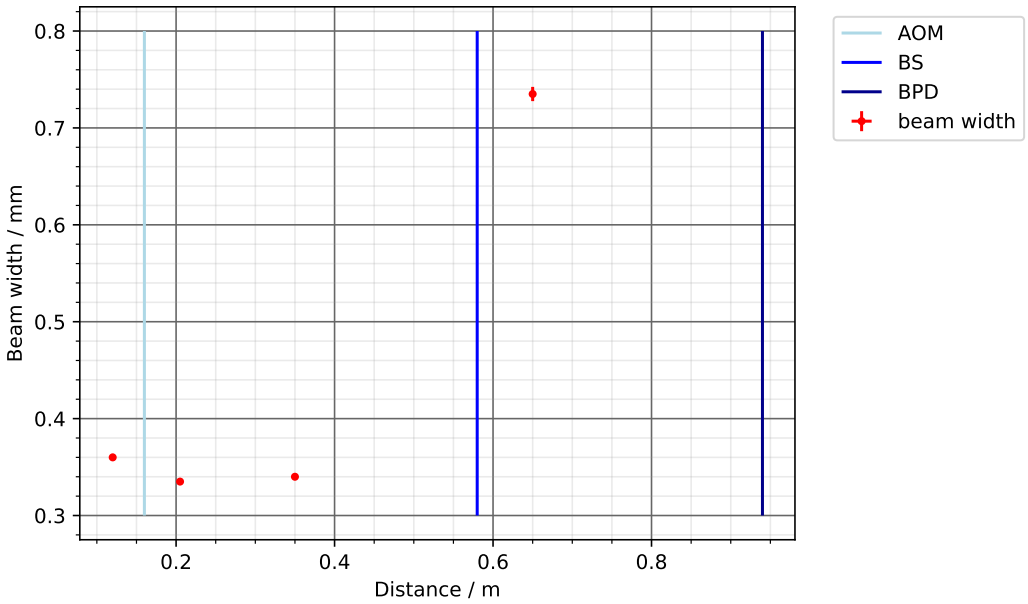

Figure 3.14: Beam profile taken with a camera over the length of the setup, with positions of AOM, BS, and BPD given, where y describes the beam width and x describes the position in the setup.

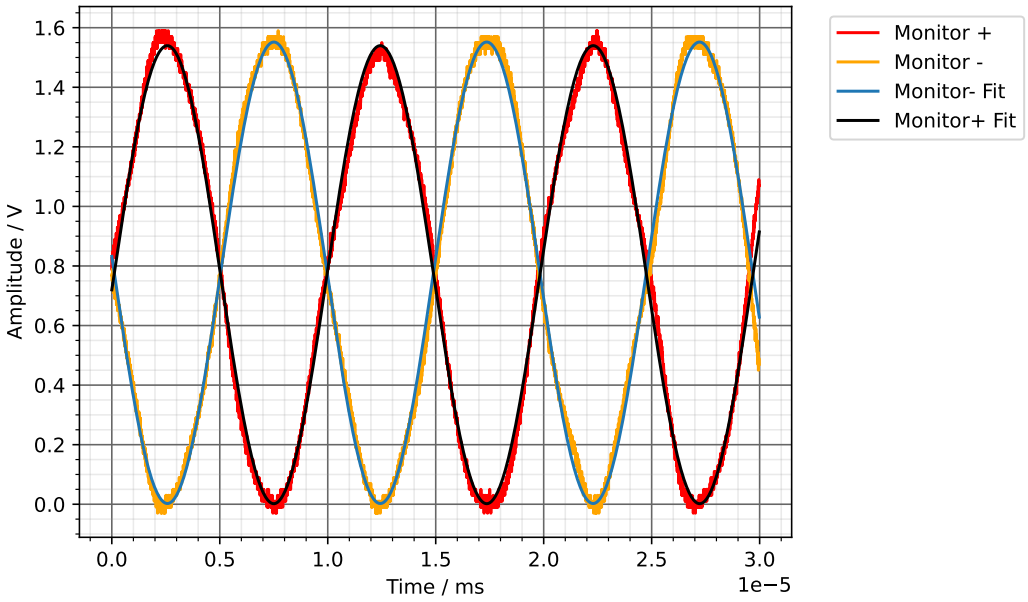

Figure 3.15: Interference fringes for the 50:50 interferometer setup as described in section 3.3 for both Monitor + and - outputs measured with an oscilloscope and their respective fit functions as $y = A \sin(fx + \phi) + c$, used as a merit for optimizing the mode matching

Calculating laser powers I will use ND plates in order to attenuate the laser beam. As it becomes increasingly difficult to measure the laser powers and the given attenuation of the plates is wavelength dependent, I measured the resulting power after the attenuation and used this to calculate the OD for 399 nm. I calculate the beam powers when using different ND filters with the calibration values

Table 3.4: Calibrated attenuation factors of a set of ND filters used for calculating the beam powers for a given power input

Given OD	Measured OD
0.5	(0.49 ± 0.01)
1	(1.04 ± 0.01)
2	(2.54 ± 0.01)
3	(3.90 ± 0.01)

enclosed in Table 3.4 using the expression:

$$I_{\text{at}} = I_{\text{in}} * 10^{-\text{OD}}. \tag{3.19}$$

Creating visibility predictions I can now use the prediction model in addition with the calculated laser powers to plot the prediction of the RF signal corresponding to the probe power for different attenuation factors. One of the plots is seen in Figure 3.16, the rest of them are in section B.1. I use the amplitude as a measure of quality for the mode matching.

3.4 Heading towards homodyning

With the previous steps taken I now replace the 50:50 with the 99:1 beam splitter to figure out how much I can attenuate the probe beam before loosing the interference signal to it's noise. Additionally I check the phase stability of the entire setup.

3.4.1 Approaching the few-photon regime

We now aim to see what the lowest beam power is, which can still be distinguished. For this I use the realigned setup with the 99:1 BS in addition with the ND plates. The taken data can be seen in section B.2. Let us look at an example measurement, seen in Figure 3.17. This shows the visibility when using a OD = 2.0 ND plate. The values for the fits are given in Table 3.5. From this I can compare the amplitude of (0.178 ± 0.001) V to the prediction in Figure 3.16 and can see, that the alignment is almost optimal as the measured value is very close to the expected maximum of 0.18 V. Comparing the amplitudes given in Table 3.5 with their expected maximums in section B.1 we can see that for lower laser powers, the measured amplitudes become smaller than the expected ones. Looking at an example using a OD = 5.0 ND plate, seen in Figure 3.19 and Figure 3.18, we can see that the measured value of (1.1 ± 0.1) mV is much smaller than the predicted 2 mV. This might be due on one hand to the noise getting larger, and on the other hand to increasing the alignment difficulty.

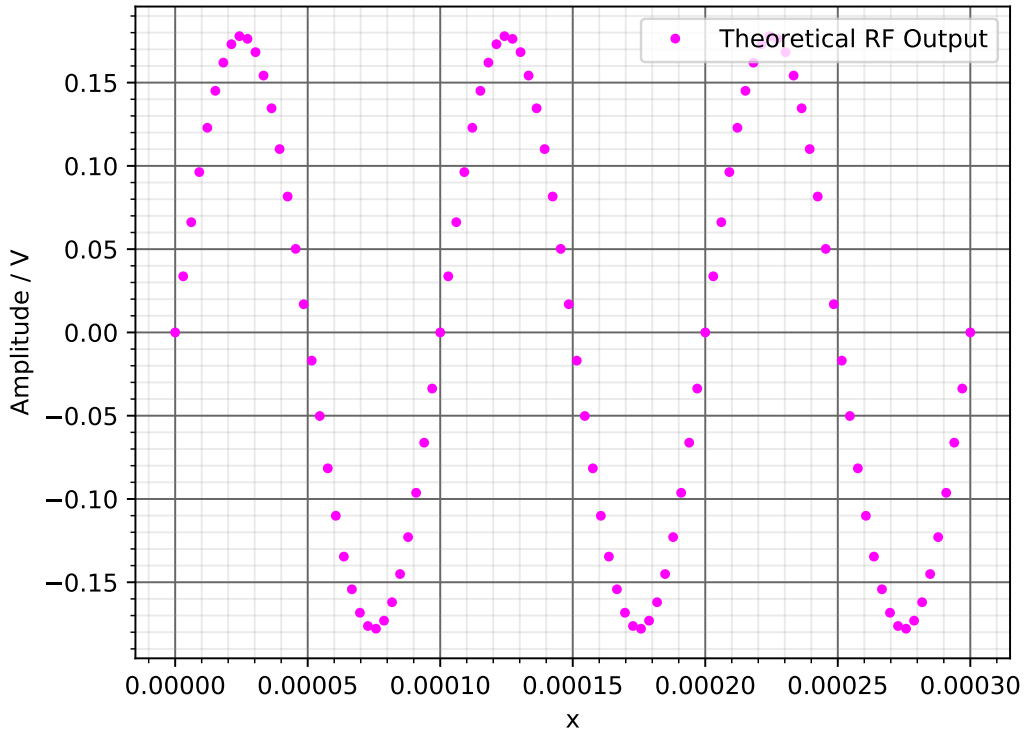

Figure 3.16: Visibility predictions of (63 ± 4) nW using the model explained in subsection 3.3.2, x is given in arbitrary units. This figure shows the theoretical maximal visibility, which can be compared to the achieved visibility in Figure 3.17

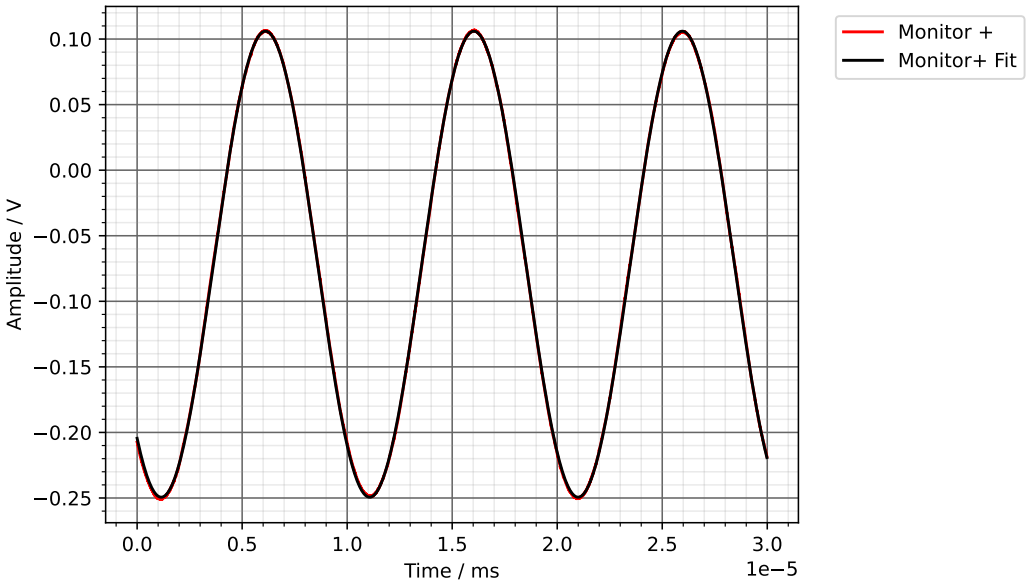

Figure 3.17: Measured visibility with setup from section 3.4 and fit data in Table 3.5 for OD = 2 0, used to calculate the Signal to Noise Ratio

Table 3.5: Fit data for measured Probe beam attenuation in section B.2, where ND plates are used to reduce the power of the Probe beam, using a detuning of 100 Hz to visualize the interference fringes

Attenuation			Amplitude A / V	Frequency $\omega = 2\pi F$ / a.u.	Shift ϕ / a.u.	Constant c / V
OD	OD_{meas}	power				
0	–	$(22 \pm 1)\,\mu W$	3.3448 ± 0.0009	$632\,866 \pm 30$	3.118 ± 0.001	-0.0771 ± 0.0006
0.5	(0.49 ± 0.01)	$(7.1 \pm 0.4)\,\mu W$	1.88615 ± 0.00033	$629\,956 \pm 20$	3.190 ± 0.001	-0.07633 ± 0.00023
1.0	(1.04 ± 0.01)	$(2.0 \pm 0.2)\,\mu W$	1.00608 ± 0.00011	$622\,401 \pm 12$	3.372 ± 0.001	-0.07372 ± 0.00008
1.5	(1.53 ± 0.02)	$(0.65 \pm 0.04)\,\mu W$	0.56888 ± 0.00007	$635\,692 \pm 13$	3.286 ± 0.001	-0.07574 ± 0.00005
2.0	(2.54 ± 0.01)	(63 ± 4) nW	0.177695 ± 0.000017	$633\,157 \pm 12$	3.986 ± 0.001	-0.071707 ± 0.000013
2.5	(3.03 ± 0.02)	(21 ± 2) nW	0.099213 ± 0.000014	$627\,137 \pm 16$	-0.176 ± 0.001	-0.071867 ± 0.000010
3.0	(3.90 ± 0.01)	(2.8 ± 0.2) nW	0.038690 ± 0.000005	$627\,732 \pm 16$	1.857 ± 0.001	-0.004653 ± 0.000004
3.5	(4.39 ± 0.02)	(0.90 ± 0.05) nW	0.022010 ± 0.000005	$624\,458 \pm 27$	-1.075 ± 0.001	-0.004518 ± 0.000004
4.0	(4.94 ± 0.02)	(0.25 ± 0.02) nW	0.012367 ± 0.000005	$626\,090 \pm 50$	1.639 ± 0.001	-0.0047546 ± 0.0000034
4.5	(5.43 ± 0.02)	(82 ± 5) pW	0.005497 ± 0.000004	$627\,170 \pm 80$	0.778 ± 0.002	-0.0040399 ± 0.0000028
5.0	(6.44 ± 0.02)	(8.0 ± 0.5) pW	0.0010749 ± 0.0000028	$628\,550 \pm 300$	0.142 ± 0.005	-0.0038723 ± 0.0000020
5.5	(6.93 ± 0.02)	(2.5 ± 0.2) pW	0.0005154 ± 0.0000024	$617\,700 \pm 600$	-0.372 ± 0.009	-0.0036352 ± 0.0000017
6.0	(7.48 ± 0.02)	(0.73 ± 0.05) pW	0.0002836 ± 0.0000023	$627\,000 \pm 1\,000$	-0.855 ± 0.016	-0.0036283 ± 0.0000017

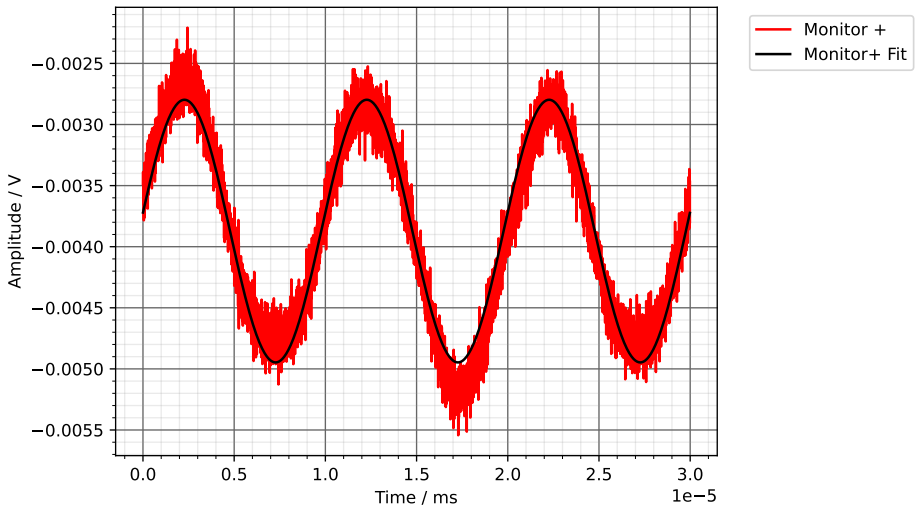

Figure 3.18: Measured visibility with setup from section 3.4 and fit data in Table 3.5 for OD = 5.0, used to calculate the Signal to Noise Ratio

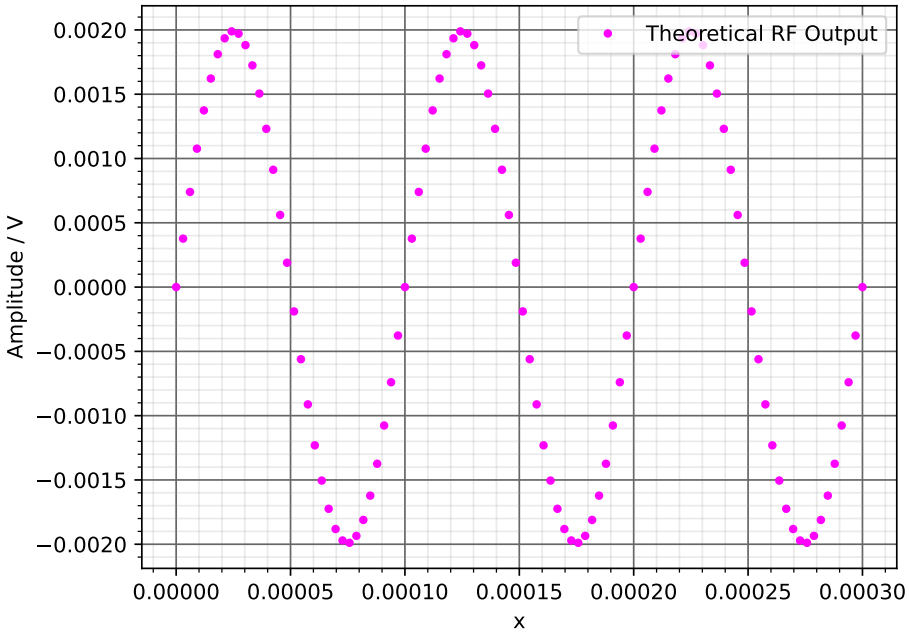

Figure 3.19: Visibility predictions of (63 ± 4) nW using the model explained in subsection 3.3.2, x is given in arbitrary units. This figure shows the theoretical maximal visibility, which can be compared to the achieved visibility in Figure 3.17

3.4.2 Detection limit in the few-photon regime

We want to be sensitive to single photons being emitted in microsecond intervals. For this we need to see how low it is possible to attenuate the beam whilst still being able to distinguish signal and noise. A merit for this is the Signal to Noise Ration (SNR), given by

$$\mathrm{SNR} = \left(\frac{P^{\mathrm{RMS}}_{\mathrm{signal}}}{P^{\mathrm{RMS}}_{\mathrm{noise}}}\right) = \left(\frac{U^{\mathrm{RMS}}_{\mathrm{signal}}}{U^{\mathrm{RMS}}_{\mathrm{noise}}}\right)^2 . \tag{3.20}$$

The lower this value, the longer we need to average to detect a signal. If the value drops below 1, the signal becomes noise dominated. SNR values of Magnitude SNR $\geq 10\,\mathrm{dB} = 10$ are considered to be measurable, whilst lower values can be improved by averaging [12]. As we assumed the noise of the signal to be dominated by the local oscillator noise, which is unchanged over the measurements, I took a measurement with the probe beam blocked in order to estimate the noise for the measurements (see Figure 3.20). The measured noise signal is$V^{\mathrm{RMS}}_{\mathrm{noise}} = (0.59 \pm 0.01)\,\mathrm{mV}$. Converting the amplitudes A from Table 3.5 to $\mathrm{V}^{\mathrm{RMS}} = \frac{1}{\sqrt{2}}\mathrm{V}$ I calculate the SNR value for each laser power. As we are interested in looking at the few-photon regime, I convert the laser power to Photons/µs using

$$\frac{\mathrm{Photons}}{\mu\mathrm{s}} = \frac{W}{hf} \tag{3.21}$$

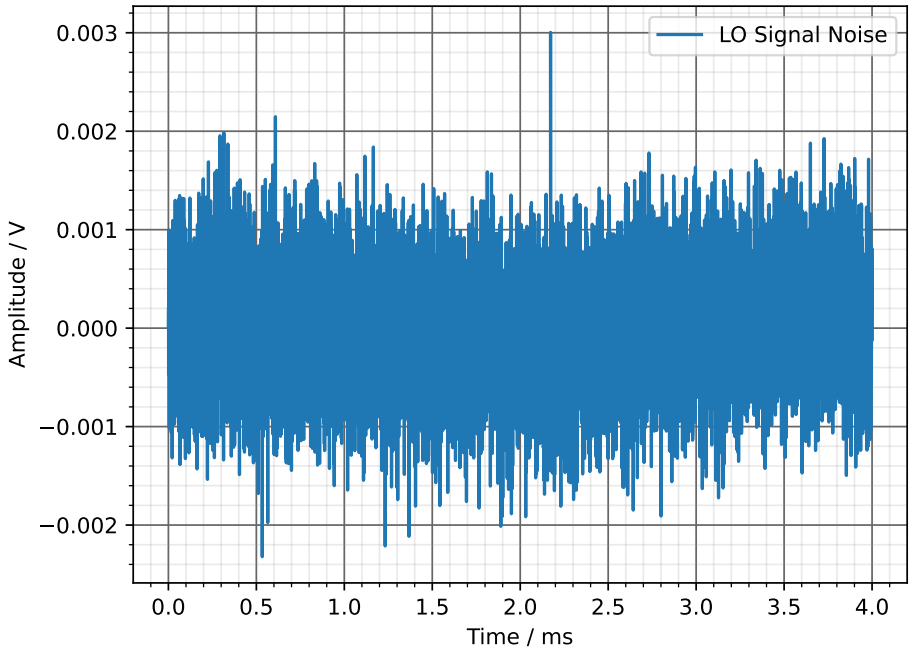

Figure 3.20: Noise measurement of the local oscillator at 3 mW

as this gives us a more intuitive understanding of how many photons are present at any given time. With this I can plot the SNR as a function of the photon rate to see how the SNR behaves for decreasing rates (see Figure 3.21). From the plot we can see that the signal is noise dominated at roughly 100 photons/µs. Using the fact that photons travel at the speed of light I can calculate, that there are on average 0.33 photons in a meter of length, which, as the detector setup is only ≈ 0.95 m long, already counts as few-photon levels. This shows great promise for the process of homodyning, as even without any further improvements on this we can already detect signals at few-photon levels. Furthermore it is possible to further improve these values, as will be discussed in chapter 4, allowing us to reach even lower photon rates and therefore greatly reduces the amount of averages needed to be taken for further measurements.

3.4.3 Interferometer phase stability and passive phase scan

For the reconstruction of the quantum state we have two key phase requirements, one is short term stability within 100 µs, as this is the scale at which the measurements will be taken, and the other is a slow drift over the span of a few hours, with which the full 360 deg of the LO phase can be scanned. For this I remove the detuning between the LO and Probe beam by driving both AOMs at 200 MHz (see Figure 3.1), as this allows us to see the phase drift of the interferometer. I first measure over a time frame of 4 000 s (see Figure 3.22). We can see that there are two timescales of phase drift, one over short duration and one over long duration. The long duration shift repeats over a time of $(1\,050 \pm 50)$ s. This allows us to passively scan the phase instead of needing to actively scan using the AOMs. One essential thing that still needs to be checked is the phase drift over the short measurement periods. It is of key importance that the phase over short measurement periods is stable enough. Should this not

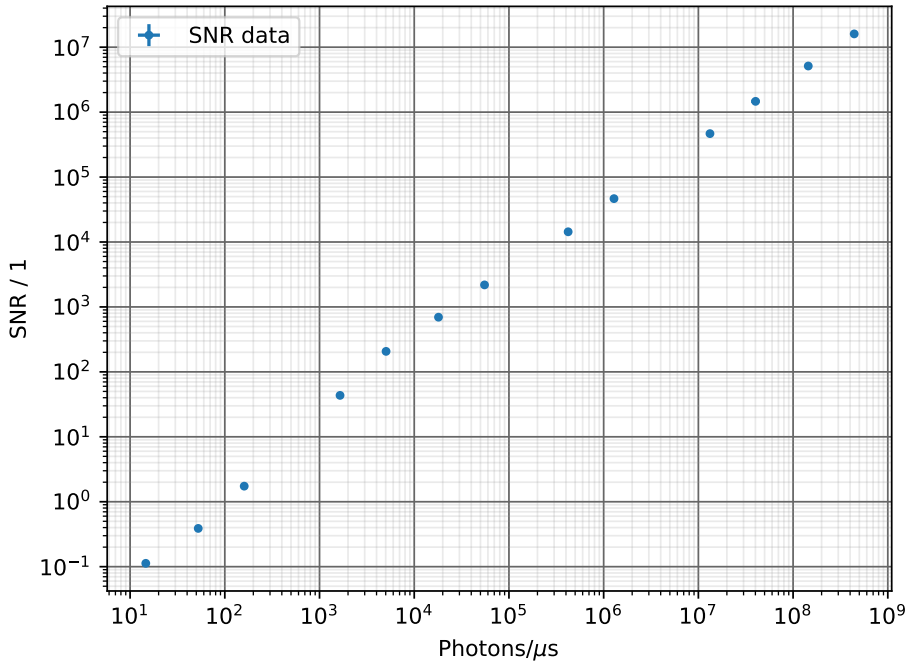

Figure 3.21: SNR for different photon rates. Lower values for the SNR will lead to more measurements, as the data points need to be averaged more. For values close to SNR = 1 we are already in the few-photon regime.

be the case, steps need to be taken in order to stabilize the perturbations which cause the short scale phase drifts. If the phase is stable over 100 µs it is possible to take measurements for specific phases and thus, using the passive phase drift over long periods, it is possible to scan the entire phase of the Local Oscillator.

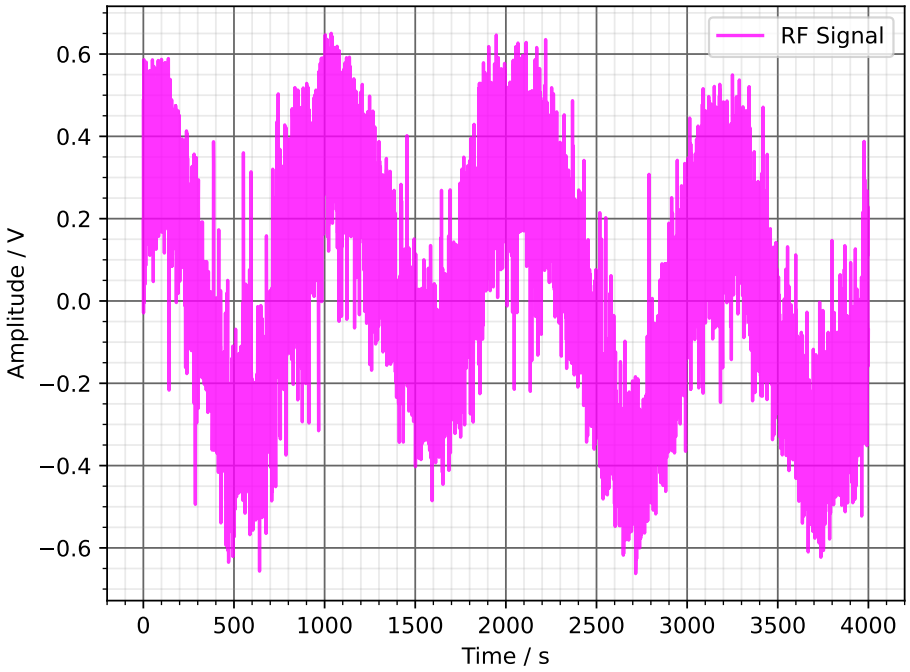

Figure 3.22: Phase drift of the Interferometer without detuning of Local Oscillator and Probe beam, measured over a time frame of 4 000 s. There are two visible drifts, one over short duration's which corresponds to the broadening of the signal, and the drift over long duration's, which shows that it is possible to scan the full phase of the Local Oscillator

CHAPTER 4

Conclusion and Outlook

We wanted to show that it is possible to create a homodyne detector for 399 nm laser light. For this I first characterized a balanced photo diode by comparing measured conversion gains for the direct PD monitor outputs and the subtracted RF Output in Table 3.2, to see that there are some small deviations from the specifications, which reduce the total amplification of the RF Output. I also calculated that the quantum efficiency of the photo detector lies at 46.6 %, which is drastically lower than for the infrared with 80.2 %. I calculated the shot noise of the checked noise spectra to verify that we are shot noise limited for the used local oscillator power of up to 2 mW. Using a 50:50 beamsplitter and a detuning of 100 MHz between the Probe and LO beam I achieved a visibility of (99.7 ± 0.1) % for the interferometer, which I then used to create a prediction model to assist with the alignment of the interferometer for low probe beam powers. Moving to the 99:1 beam splitter I used ND-plates to attenuate the probe beam to low powers and found, that the limit at which the signal could still be distinguished from the noise lies at 100 Photons/µs for the used setup. Lastly, I took a long measurement without the detuning over 1.25 h to see that it is possible to passively scan the phase of the local oscillator. One last measurement that still needs to be taken is the phase stability for time frames of a few hundred microseconds, as this is the time window where the measurements leading to state reconstruction will be taken.

4.1 Resolvable photon flux

Using the created prediction model to align the interferometer and ND plates to attenuate the beam I could measure signals down to 100 Photons/µs, at which point the noise becomes dominant over the signal. Considering the length of the interferometer,this corresponds to the few-photon regime. This already provides the possibility to take measurements in the few-photon regime. Improving the Signal to Noise Ratio would allow us to reduce the needed measurements, as less averages would be required to get an equal or better SNR. A limiting factor for the resolvable signal level in my setup is the utilized oscilloscope which cannot resolve signals lower than 0.1 mV. Using a measuring device that can resolve lower signals would allow us to achieve an even smaller photon flux. Alternatively a different detector with a higher amplification and better noise performance could be used. As we only use frequencies up to 10 MHz for the calculations, a low-pass filter to cut out higher frequency noise can be used to reach even lower Probe beam powers. In addition, to reduce the noise coming from the detector, the setup can be properly isolated from it's surroundings to reduce the impact

of outside noise, like stray light which introduces white noise, air currents which slightly shift the refraction index of the air, temperature changes or mechanical vibrations which vary the lengths of the interferometer arms, etc.

Quantum Efficiencies The quantum efficiency of the detector itself lies at 46.6 % for 399 nm laser light. This can largely be seen in the form of reflected light coming off of the detector itself. In comparison to the efficiency at 820 nm of $QE(820\,\text{nm}) = 80.2\,\%$, this is rather low. We are interested in increasing this efficiency, as this would mean that when using single photon sources we would loose more than half of all incoming photons at the detector, and thus requires more time for measurements. One way of increasing it is by refocusing the reflected light back onto the detector, which could increase the quantum efficiency by an additional fraction of the quantum efficiency. A simpler solution would be to use specific photo diodes for blue laser light, which intrinsically come with a higher quantum efficiency at the used wavelength.

Homodyne detection at 399 nm From the results of this thesis we can see that it is possible to measure signals in the few-photon regime. The phase of the setup also drifts enough with time that it allows us to passively scan the different phases. One last thing which is needed to be checked is if the phase stability over 100 µs is stable. If this is the case it would allow us to perform homodyne detection for the blue. Therefore the next steps towards the reconstruction of wigner functions and density matrices can be taken. For this, a data acquisition method should be implemented, because when heading for the total state reconstruction we require a lot of measurements. These consist of short duration measurements in the region of a hundred microseconds. Each measurement corresponds to a single point of data for a specific phase of the local oscillator. This should be repeated a few thousand times in order to get a properly averaged result for one phase. This then also needs to be repeated for multiple different phases of the local oscillator. It is therefore required to setup automated data acquisition methods. We plan on using a Data Acquisition Card[1] for this process.

After setting up the data acquisition the data needs to be fed into an algorithm, the Maximum likelihood estimation algorithm, which is described by A. I. Lvovsky [13]. This needs to be programmed and test, as it is needed to recreate Wigner and Density functions. Finally, with a working algorithm these can be recreated. This should be done first for vacuum and coherent states to see if it is possible to recreate the expected results. If the expected results are verified, the setup can be implemented into the YQO Experiment. As the experimental setup itself runs on specific timings and pulsed lasers, the timings of data acquisition need to be matched with the timings of the setup itself.

Finally it needs to be figured out if the setup is to be run by locking the interferometer and manually setting a phase, e.g. using EOMs, or by scanning passively and additionally measuring the phase for each data point. Locking the interferometer would give us control of measuring specific phases [9], but is rather complex to implement and requires at least an additional EOM and laser. On the other hand the passive scanning of the phase requires an additional simultaneous measurement to determine the phase of the measured data point.

[1] Series/Model : RazorMax / CompuScope Express 16502

APPENDIX A

Measuring using Oscilloscope and Spectrum Analyzer

Two devices used to take and visualize data are the spectrum analyzer (DSA705[1]) and the oscilloscope (MDO3024[2]). These devices have certain properties and we use them in specific ways.

A.1 Spectrum Analyzer

We use the spectrum analyzer to take data in the frequency regime, for this we use two different settings for the ranges 0...150 MHz and 0...10 MHz . The relevant settings are resolution bandwidth, video-resolution (V/R) ratio, detection type, filter type, sweep time and trace type. We set the V/R-ratio to 0.1 as is specified by the manufacturer for noise measurements. The detection type is set to RMS AVG, and filter type "Gause". For the sweep time we use the "auto accy" option for higher precision measurements and the trace type "power avg". For 0...10 MHz we use a resolution band width of 10 kHz and for 0...150 MHz we use 30 kHz

A.1.1 Data processing with the Spectrum Analyzer

As we wish to further process the measured data we need to know how the data is taken. The taken data is given in dBm instead of dBm/Hz, as the analyzer integrates over the bin width for each data point. In order to integrate over a relevant part of the spectrum we first need to transform our data back to dBm/Hz. We do this by dividing the data by the resolution bandwidth. Now in order to properly integrate over the range, we convert dBm/Hz to W/Hz and multiply by the bin width to get an area which we can then integrate up to the point of our choosing to get a single noise power value for the entire spectrum.

[1] URL: https://www.batronix.com/shop/spectrum-analyzer/Rigol-DSA705.html
[2] URL: https://www.tek.com/en/products/oscilloscopes/mdo3000

APPENDIX B

Attenuation of probe beam

B.1 Prediction plots

Here follow the plots for the prediction model.

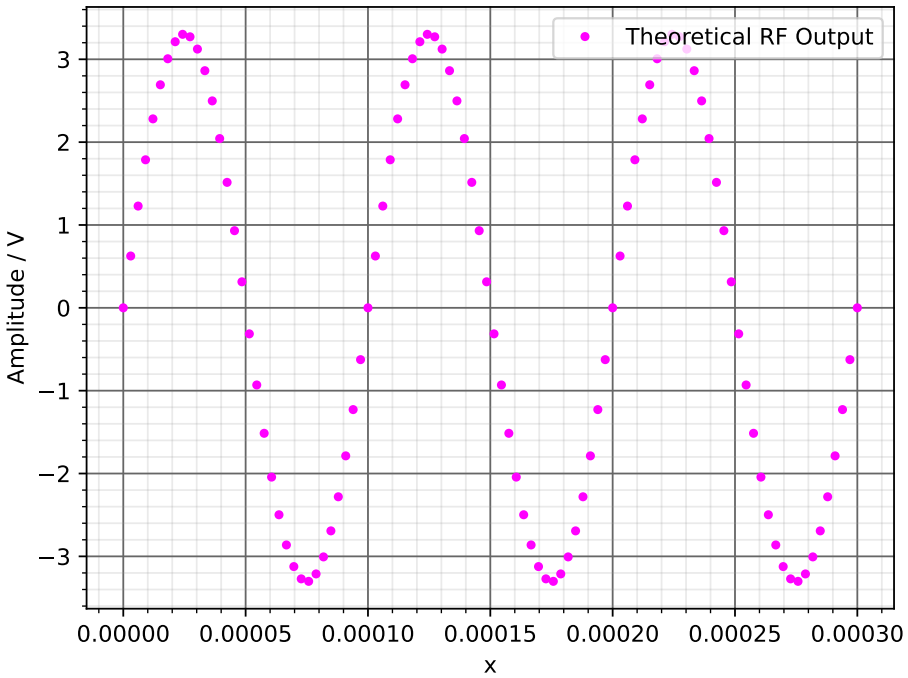

Figure B.1: Visibility predictions of $(22 \pm 1)\ \mu$W using the model explained in subsection 3.3.2

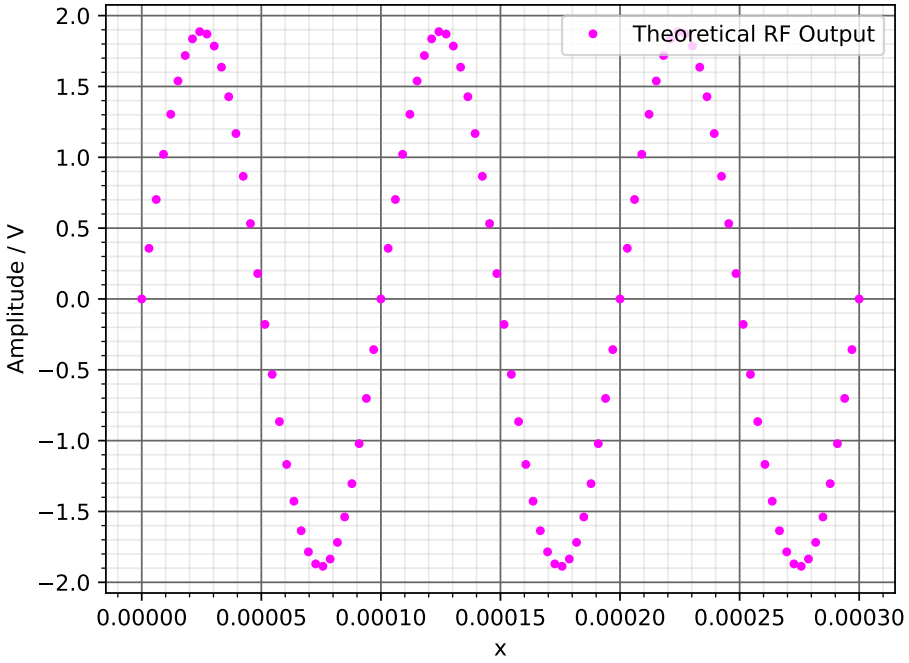

Figure B.2: Visibility predictions of $(7.1 \pm 0.4)\ \mu$W using the model explained in subsection 3.3.2

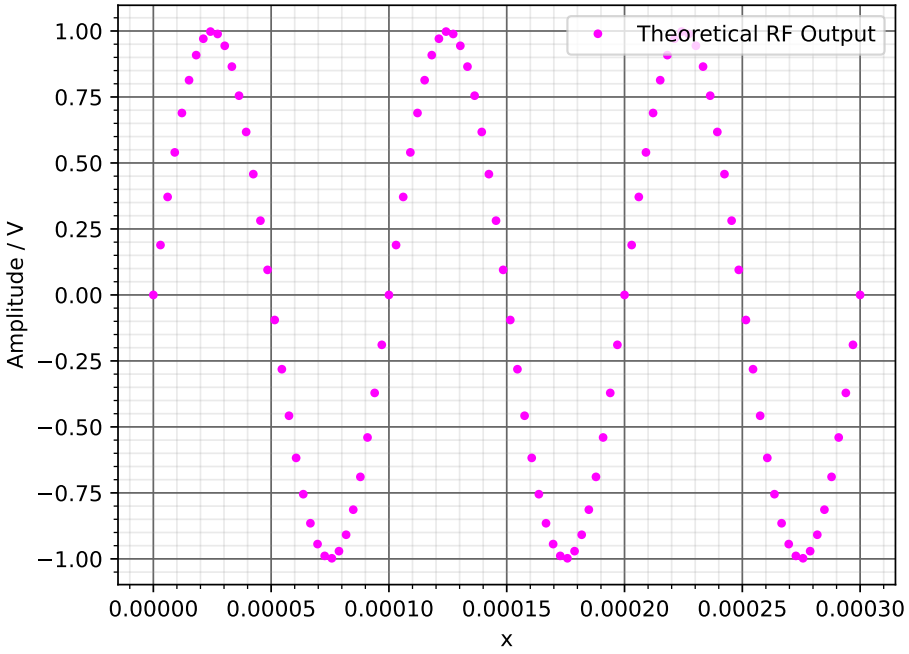

Figure B.3: Visibility predictions of $(2.0 \pm 0.2)\ \mu$W using the model explained in subsection 3.3.2

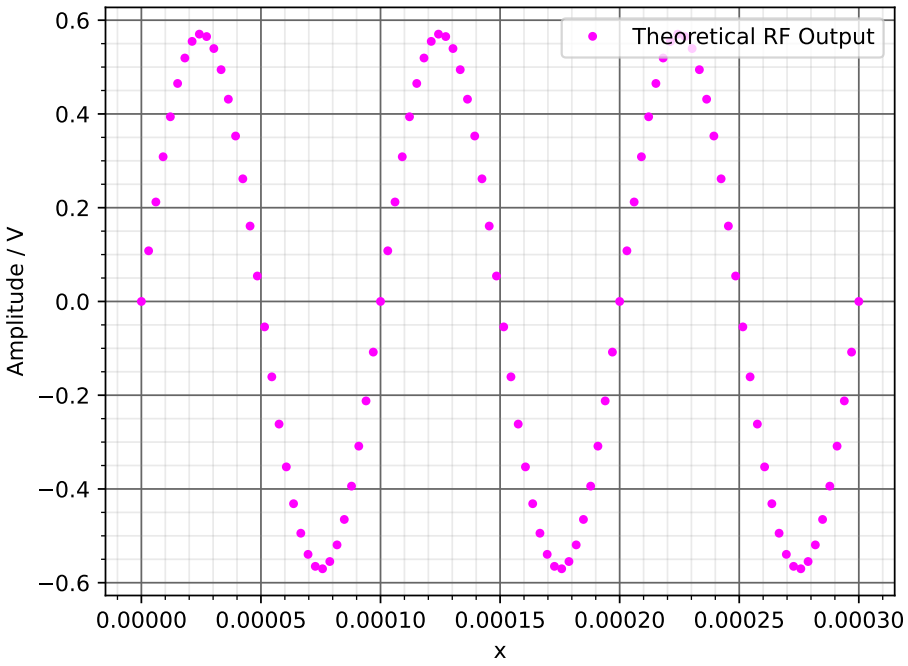

Figure B.4: Visibility predictions of (650 ± 40) nW using the model explained in subsection 3.3.2

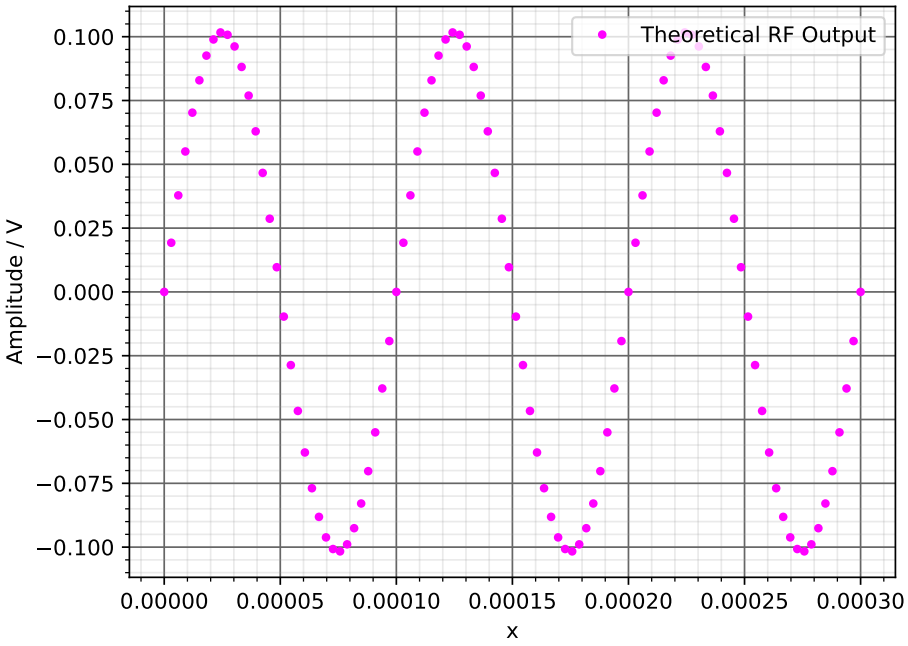

Figure B.5: Visibility predictions of (21 ± 2) nW using the model explained in subsection 3.3.2

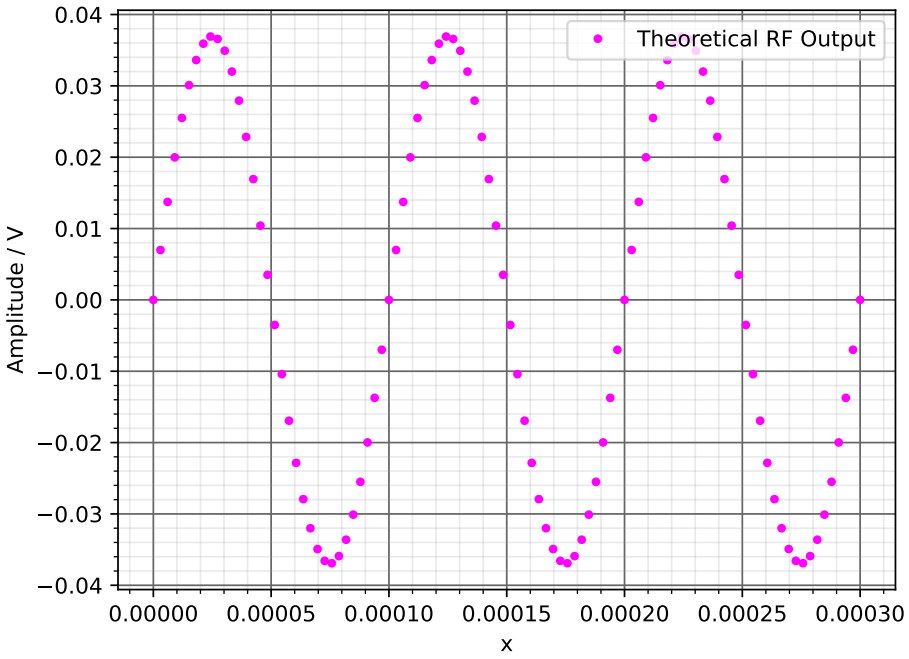

Figure B.6: Visibility predictions of (2.8 ± 0.2) nW using the model explained in subsection 3.3.2

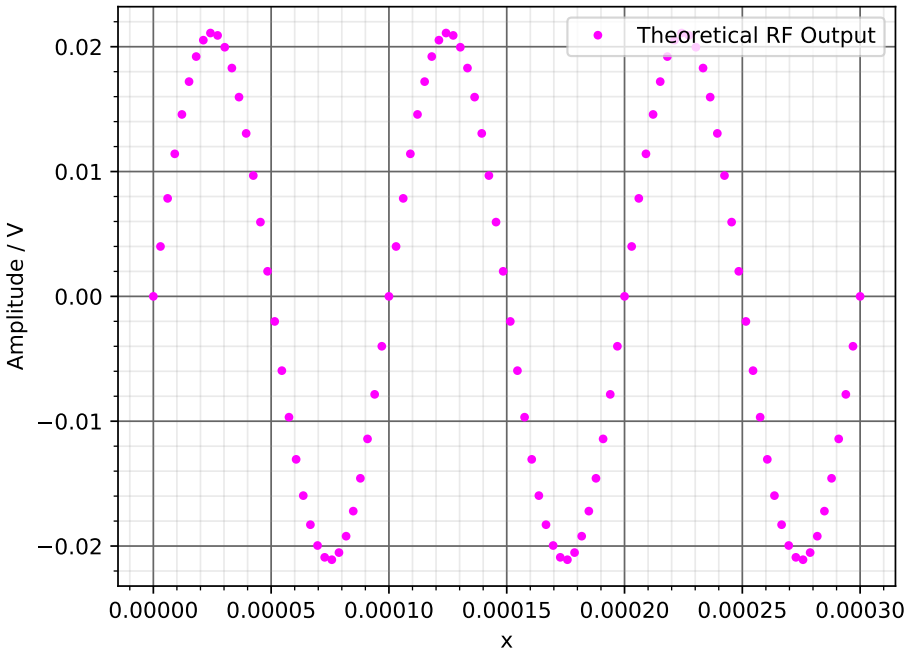

Figure B.7: Visibility predictions of (0.90 ± 0.06) nW using the model explained in subsection 3.3.2

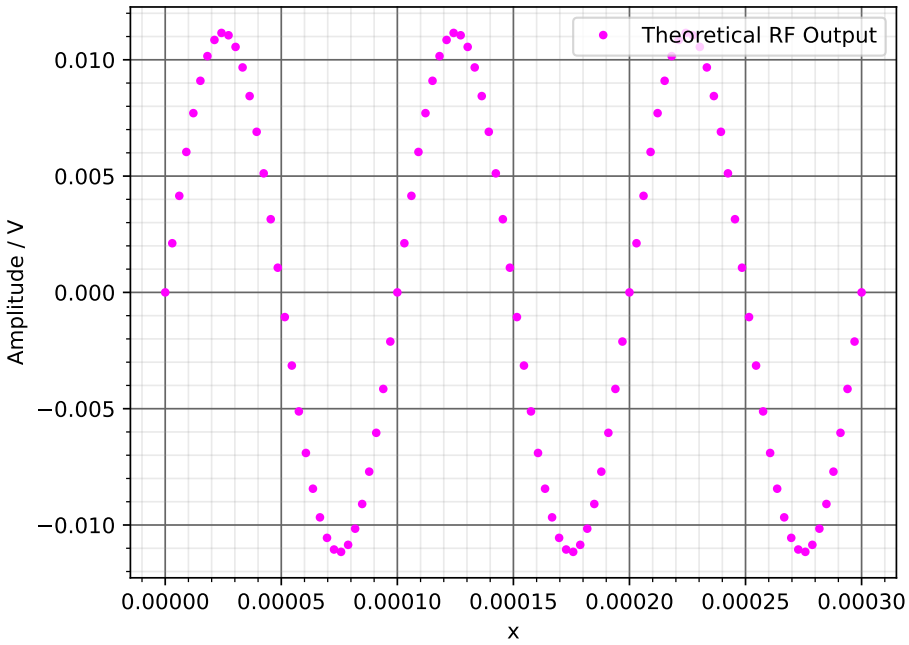

Figure B.8: Visibility predictions of (250 ± 20) pW using the model explained in subsection 3.3.2

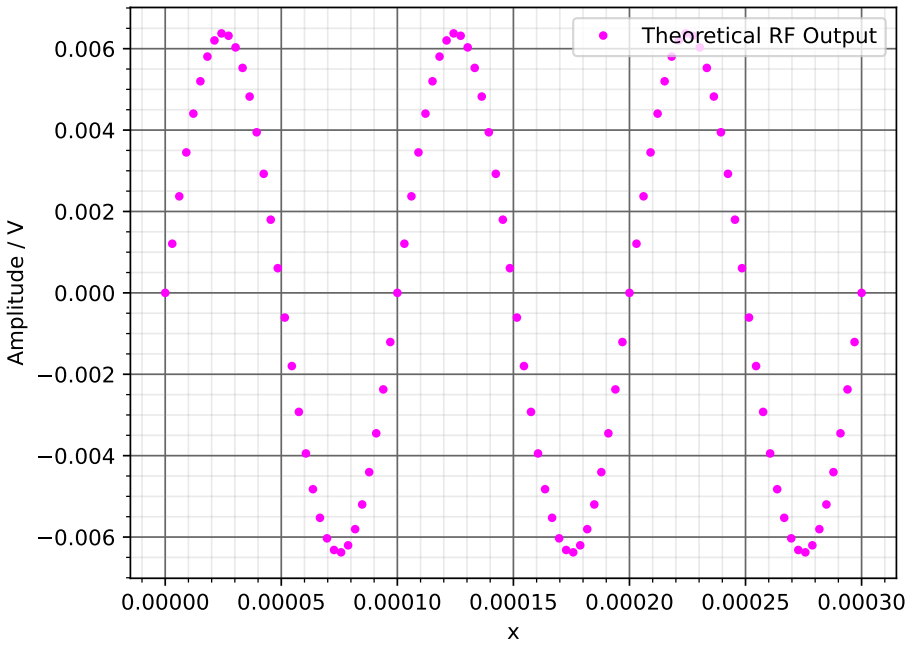

Figure B.9: Visibility predictions of (82 ± 5) pW using the model explained in subsection 3.3.2

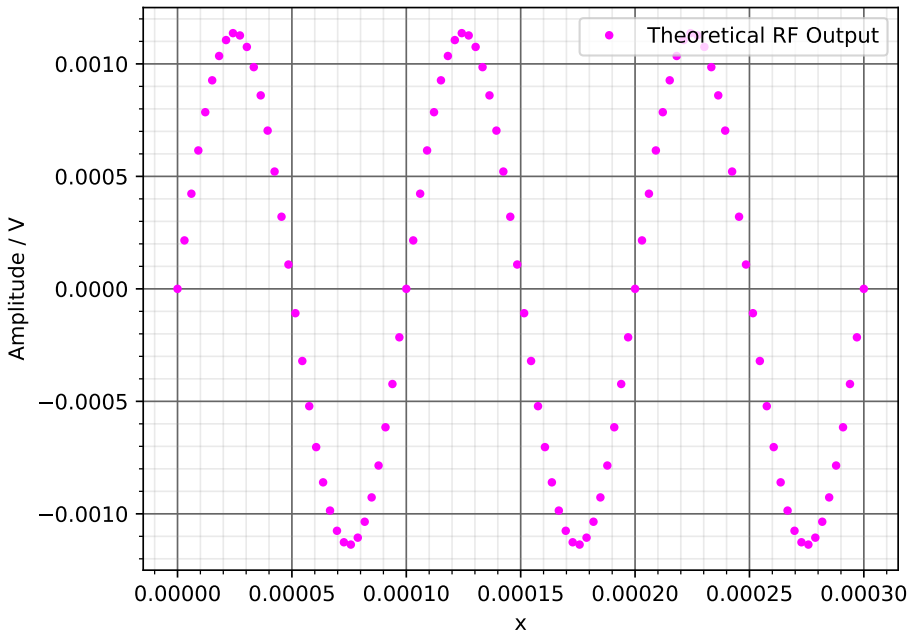

Figure B.10: Visibility predictions of (2.6 ± 0.2) pW using the model explained in subsection 3.3.2

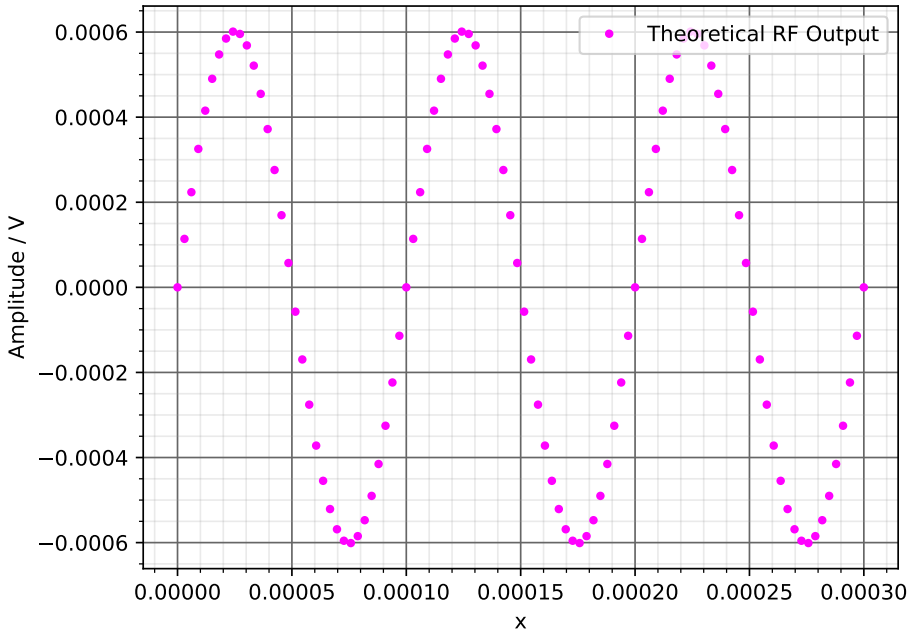

Figure B.11: Visibility predictions of (0.73 ± 0.05) pW using the model explained in subsection 3.3.2

B.2 Measured beam attenuation

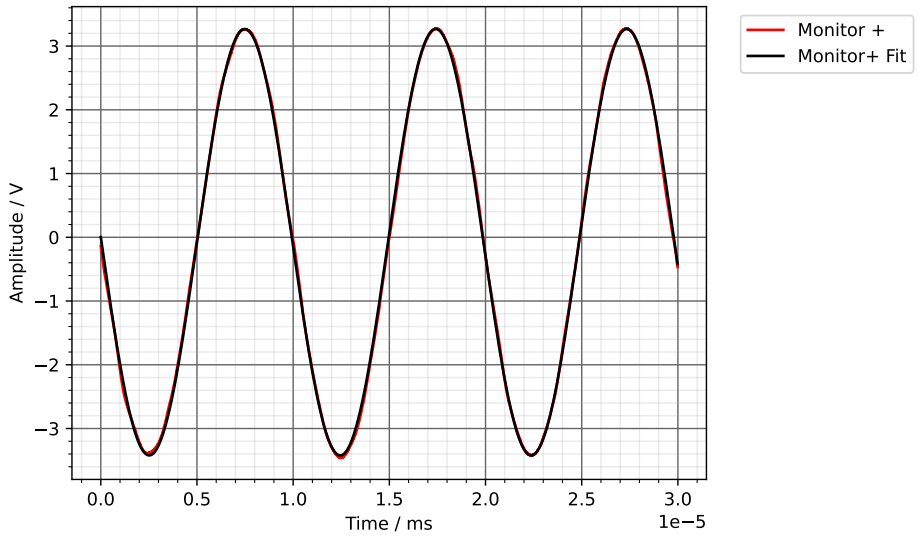

Figure B.12: Measured visibility with setup from section 3.4 and fitdata in Table 3.5 for OD = 0

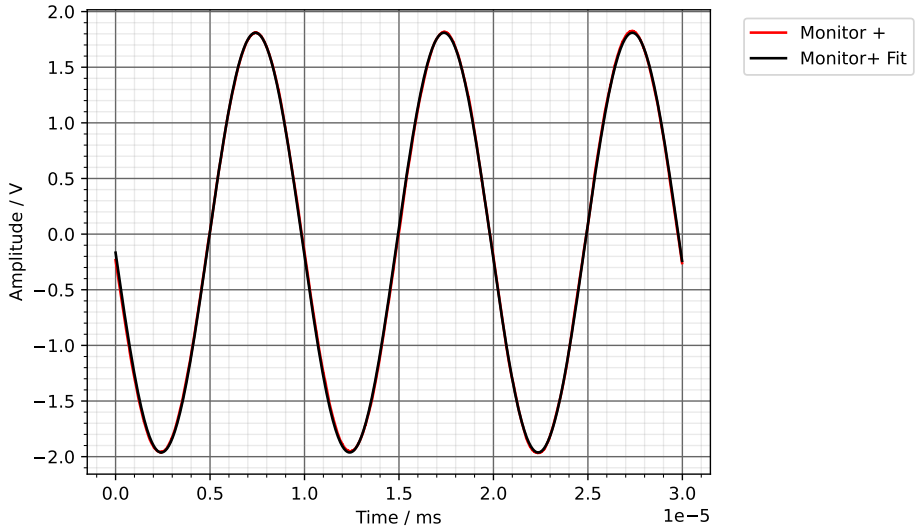

Figure B.13: Measured visibility with setup from section 3.4 and fitdata in Table 3.5 for OD = 0.5

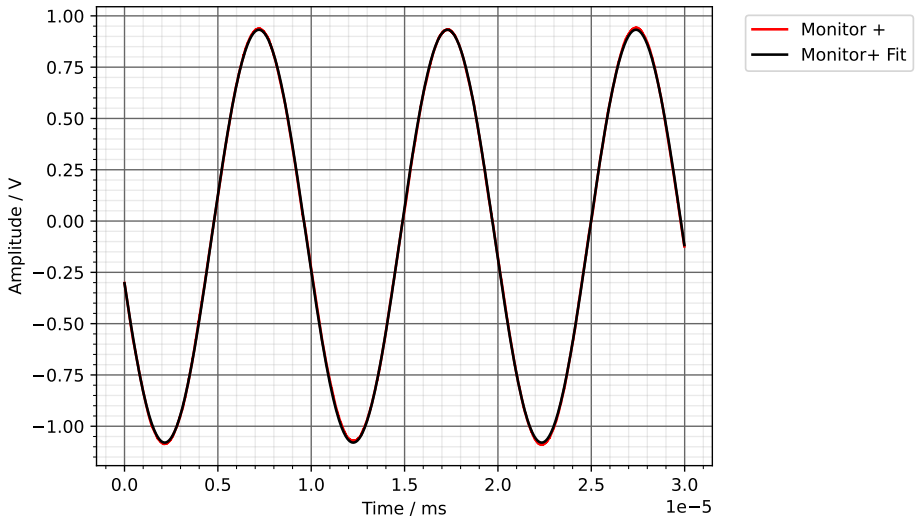

Figure B.14: Measured visibility with setup from section 3.4 and fitdata in Table 3.5 for OD = 1.0

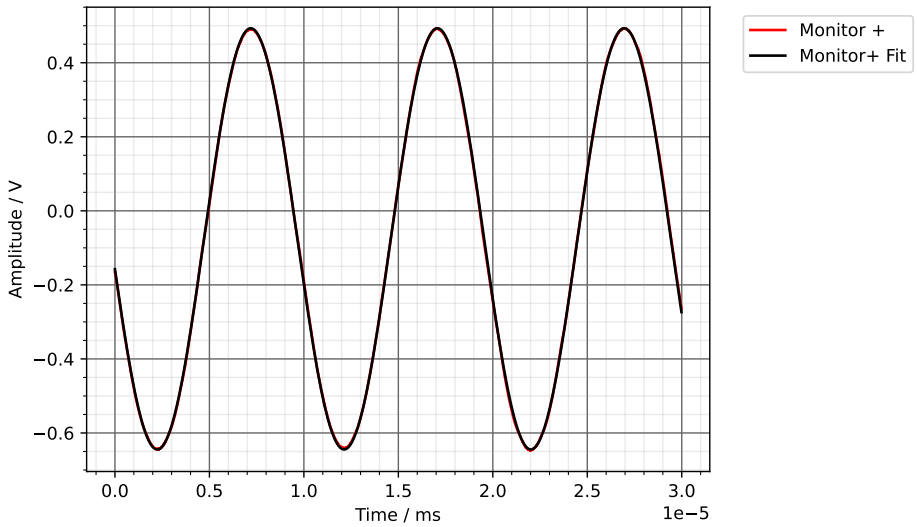

Figure B.15: Measured visibility with setup from section 3.4 and fitdata in Table 3.5 for OD = 1.5

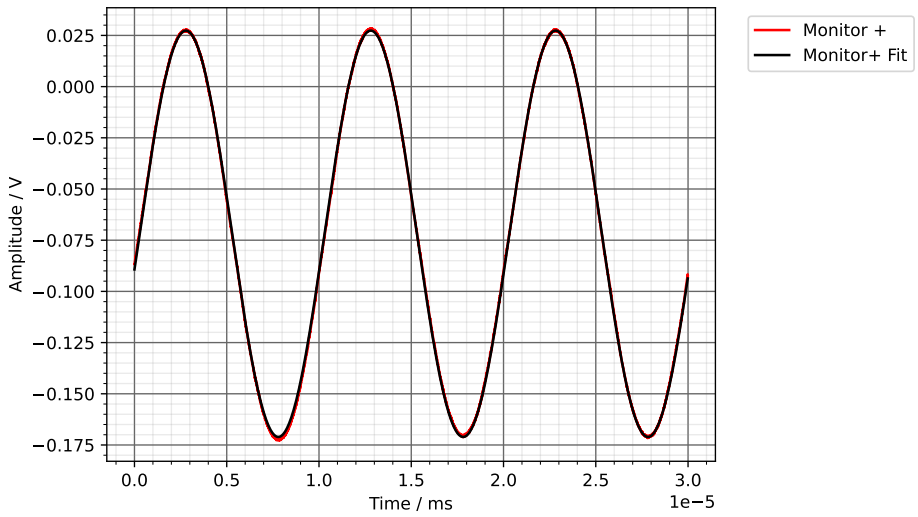

Figure B.16: Measured visibility with setup from section 3.4 and fitdata in Table 3.5 for OD = 2.5

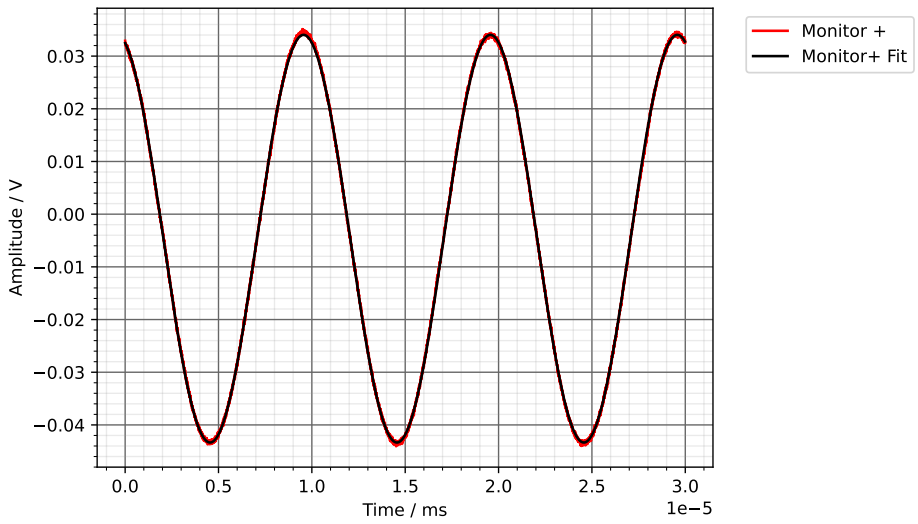

Figure B.17: Measured visibility with setup from section 3.4 and fitdata in Table 3.5 for OD = 3.0

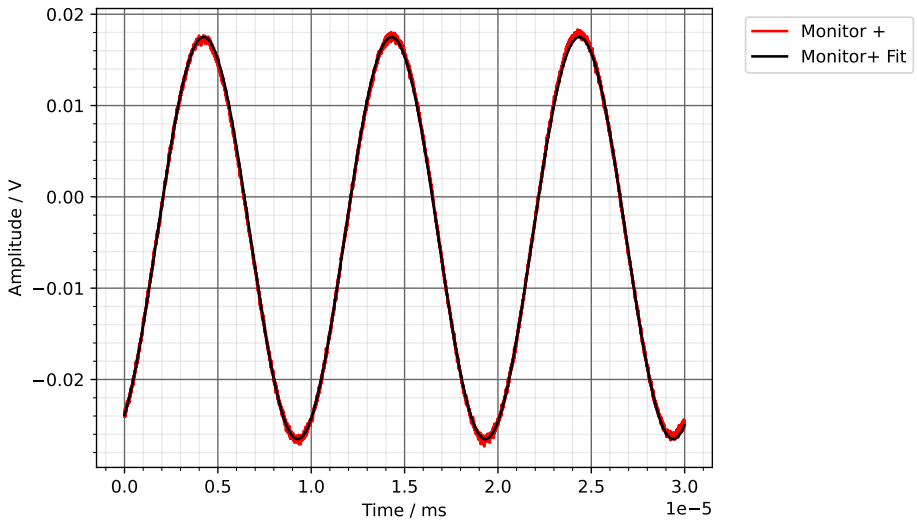

Figure B.18: Measured visibility with setup from section 3.4 and fitdata in Table 3.5 for OD = 3.5

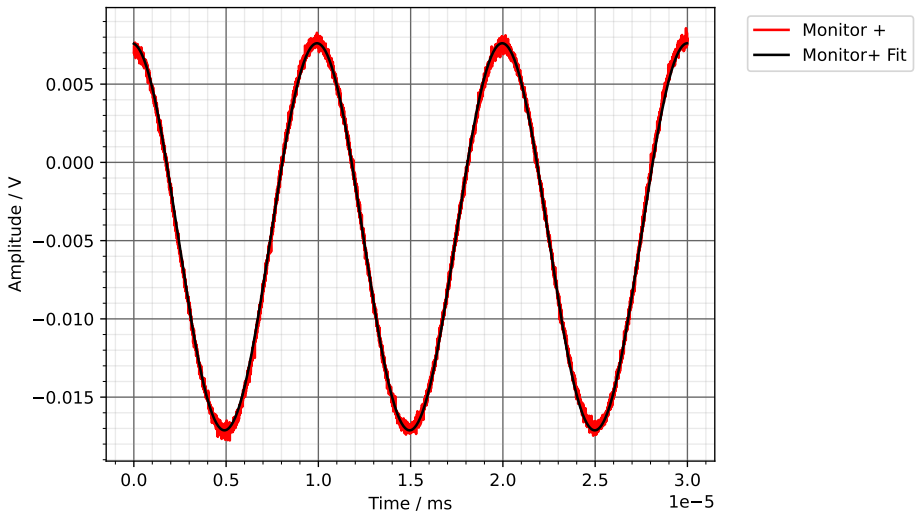

Figure B.19: Measured visibility with setup from section 3.4 and fitdata in Table 3.5 for OD = 4.0

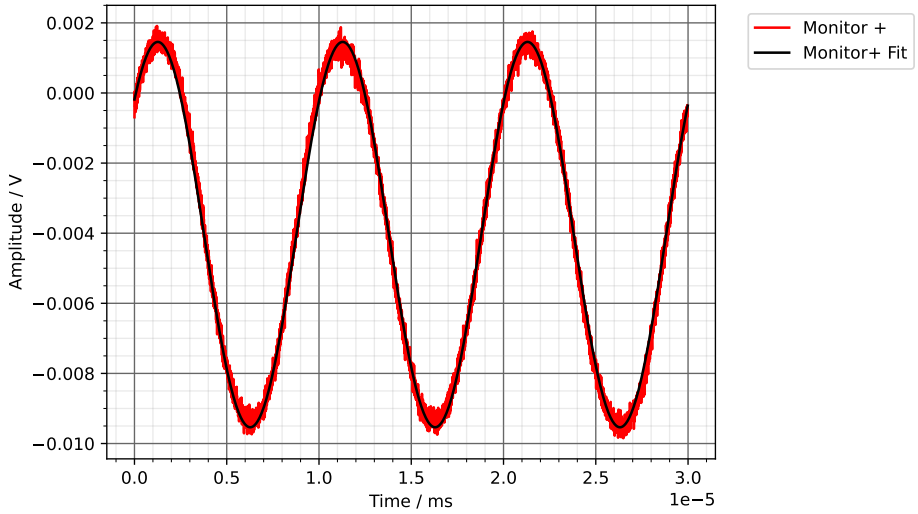

Figure B.20: Measured visibility with setup from section 3.4 and fitdata in Table 3.5 for OD = 4.5

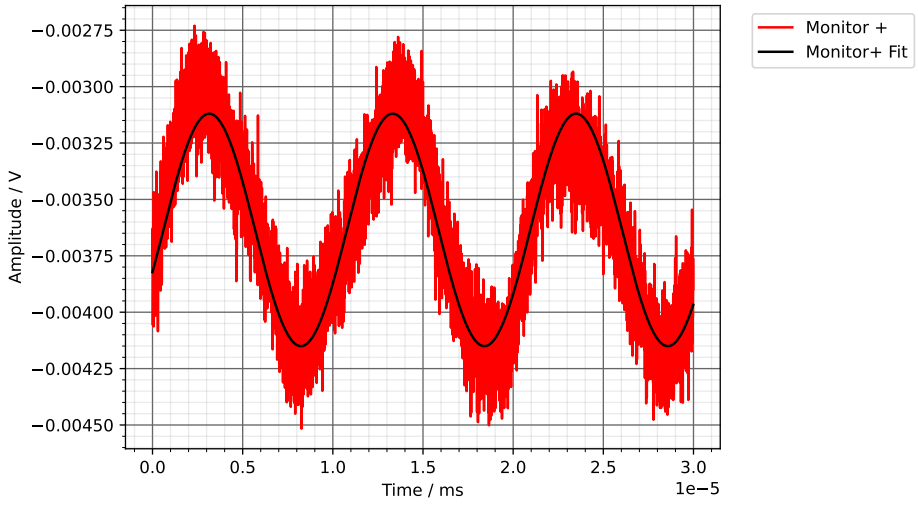

Figure B.21: Measured visibility with setup from section 3.4 and fitdata in Table 3.5 for OD = 5.5

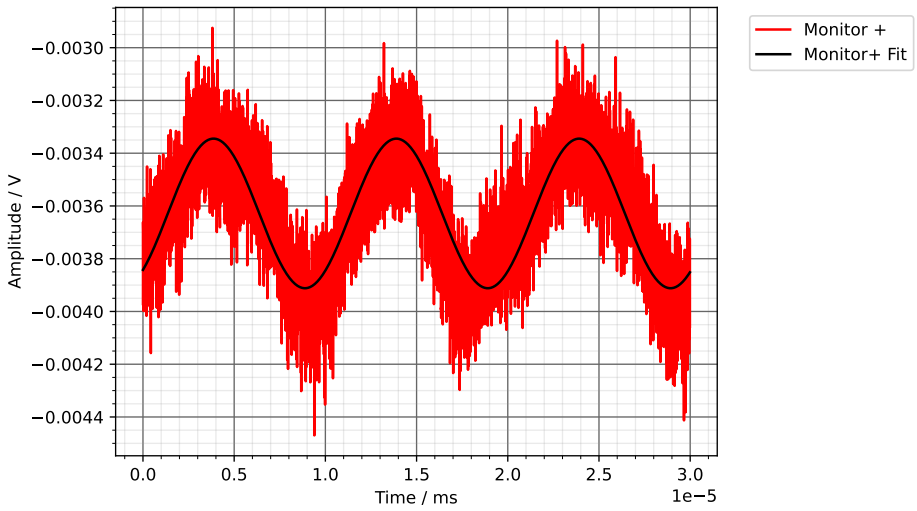

Figure B.22: Measured visibility with setup from section 3.4 and fitdata in Table 3.5 for OD = 6.0

Bibliography

[1] L. K. Grover, "A fast quantum mechanical algorithm for database search," *Proceedings of the twenty-eighth annual ACM symposium on Theory of Computing*, STOC '96, New York, NY, USA: Association for Computing Machinery, 1996 212, ISBN: 978-0-89791-785-8, (visited on 11/01/2023).

[2] *The quantum conundrum: Challenges to getting quantum computing on deck*, en, (visited on 11/04/2023).

[3] O. Firstenberg, C. S. Adams, and S. Hofferberth, *Nonlinear quantum optics mediated by Rydberg interactions*, en, Journal of Physics B: Atomic, Molecular and Optical Physics **49** (2016) 152003, Publisher: IOP Publishing, (visited on 11/04/2023).

[4] A. K. Speier, *Heterodyne interferometer for detection of conditional single-photon phase shifts*, Bachelor's Thesis, 2023.

[5] A. C. Nitsch, *Interferometer setup for detecting photon-number dependent phase shifts*, Bachelor's Thesis, 2023.

[6] M. G. Hansen, *Precision Measurements in a Rydberg Quantum Optics Experiment*, Master's Thesis, 2021.

[7] M. Rockenhäuser, *A Setup for Heterodyne Single-Photon Phase Shift Detection*, Bachelor's Thesis, 2016.

[8] J. Vaneecloo, S. Garcia, and A. Ourjoumtsev, *Intracavity Rydberg Superatom for Optical Quantum Engineering: Coherent Control, Single-Shot Detection, and Optical $\ensuremath{\pi}$ Phase Shift*, Physical Review X **12** (2022) 021034, Publisher: American Physical Society, (visited on 11/04/2023).

[9] V. Magro, J. Vaneecloo, S. Garcia, and A. Ourjoumtsev, *Deterministic freely propagating photonic qubits with negative Wigner functions*, en, Nature Photonics **17** (2023) 688, Number: 8 Publisher: Nature Publishing Group, (visited on 11/04/2023).

[10] M. Fox, *Quantum optics: an introduction*, eng, Oxford master series in physics, OCLC: 252682628, Oxford: Oxford University Press, 2006, ISBN: 978-0-19-152425-7, (visited on 11/01/2023).

[11] R. LaPierre, *Getting Started in Quantum Optics*, en, Undergraduate Texts in Physics, Cham: Springer International Publishing, 2022, ISBN: 978-3-031-12432-7, (visited on 11/06/2023).

[12] *What is Signal to Noise Ratio and How to calculate it?* en-US, 2022, (visited on 11/09/2023).

[13] A. I. Lvovsky and M. G. Raymer, *Continuous-variable optical quantum-state tomography*, Reviews of Modern Physics **81** (2009) 299, Publisher: American Physical Society, (visited on 11/05/2023).